Quarterly Report for

Contract DE-FG36-02ID14418

Stanford Geothermal Program

July-September 2003

Table of Contents

1. A CHANNEL-ORIENTED MODEL AND EXPERIMENTS FOR RELATIVE PERMEABILITIES THROUGH FRACTURES

This project is being conducted by Research Assistant Chih-Ying Chen, Professor Roland Horne and Visiting Researcher Mostafa Fourar. In this research, an experimental apparatus was built to capture the unstable nature of the two-phase flow in a smooth-walled fracture and display the flow patterns in different flow configurations real time. Air-water relative permeabilities were obtained from experiments at both room temperature and high temperature. These results showed deviation from the X-curve suggested by earlier studies. Through this work the relationship between phase-channel morphology and relative permeability in fractures was determined. A physical channel-oriented model was proposed which could replicate experimental results in both room- and high-temperature cases. Other relative permeability models (viscous-coupling model, X-curve model and Corey-curve model) are also discussed. These models could not, however, represent the experimental relative permeabilities as well as the proposed channel-oriented model. Hence, we concluded that the two-phase relative permeability in fractures depends not only on liquid type and fracture geometry but also on the two-phase flow patterns.

1.1 INTRODUCTION

Two-phase flow through fracture media is important in geothermal applications. However, the flow mechanism and the characteristic behavior of relative permeability in fractures are still not well determined. Furthermore, the knowledge of the relationship between flow behaviors and relative permeabilities in fractures is limited. Among earlier studies, it is difficult to find a single model that can provide consistent results for modeling relative permeabilities in fractures. One of the most commonly used approaches to model multiphase flow in fractures is the porous medium approach. This approach treats fractures as connected two-dimensional porous media. In this model, a pore space occupied by one phase is not available for flow for the other phase. A phase can move from one position to another only upon establishing a continuous flow path for itself. As in porous media, the competition for pore occupancy is described by relative permeability and governed by Darcy's law. Darcy's law for single-phase liquid system is:

$$u_l = \frac{k_{abs}(p_i - p_o)}{\mu_l L} \tag{1.1}$$

where subscript l stands for the liquid phase, i for inlet and o for outlet; μ, p, L, u, k_{abs} are the viscosity, pressure, fracture length, Darcy flow velocity and absolute permeability respectively.

For liquid and gas phases in two-phase flow, Eq. 1.1 becomes

$$u_l = \frac{k_{abs}k_{rl}(p_i - p_o)_l}{\mu_l L} \tag{1.2}$$

$$u_g = \frac{k_{abs}k_{rg}(p_i - p_o)_g}{\mu_g L} \tag{1.3}$$

where the subscript g pertaining to the gas phase; k_{rl} and k_{rg} are the relative permeability of the liquid and gas phases.

Scheidegger (1974) further modified Darcy's law derived for single-phase isothermal gas flow in porous media

$$u_g = \frac{k_{abs}(p_i^2 - p_o^2)}{2\mu_g L p_o} \tag{1.4}$$

In two-phase flow, Eq. 1.3 becomes

$$u_g = \frac{k_{abs}k_{rg}(p_i^2 - p_o^2)}{2\mu_g L p_o} \tag{1.5}$$

The absolute permeability of a smooth-walled fracture is a function only of the fracture aperture, *b* (Witherspoon et al., 1980) as described in the relationship:

$$k_{abs} = \frac{b^2}{12} \tag{1.6}$$

The concept of relative permeability provides us a means to quantify the relative resistance or interference between phases. For gas-water two-phase flow, the sum of the relative permeabilities, k_{rl} and k_{rg} indicates the extent of phase interference. The lower is the sum of the relative permeabilities below 1, the greater is the phase interference. Relative permeability functions are usually taken to be dependent on phase saturation. The two most commonly used expressions for relative permeability for homogeneous porous media are the X-curve and the Corey curve (Corey, 1954). The X-curve defines relative permeability as a linear function of saturation:

$$k_{rl} = S_l \tag{1.7}$$

$$k_{rg} = S_g \tag{1.8}$$

where S_l and S_g are the liquid and gas saturation respectively. The sum of X-curve relative permeabilities equals to one, which means the absence of phase interference. Physically this implies that each phase flows in its own path without impeding the flow of the other. In fractures, if each phase flows via perfect straight channels along flow direction with the negligible capillary pressure and wetting-phase stratified flow on the top and bottom surface of the fracture, X-curve behavior is possible.

The Corey curves relate relative permeability to the irreducible or residual liquid and gas saturation, S_{rl} and S_{rg} :

$$k_{rl} = S^{*4} \tag{1.9}$$

$$k_{rg} = (1 - S^*)^2(1 - S^{*2}) \tag{1.10}$$

$$S^* = (S_l - S_{rl})/(1 - S_{rl} - S_{rg}) \tag{1.11}$$

Corey curve model, which represents relative strong phase interference in comparison with X curve, is frequently used in modeling the relative permeability in porous media.

Previous work on multiphase flow in fractures includes Romm's (1966) experiment with kerosene and water through a parallel-plate smooth-walled fracture lined with strips of polyethylene or waxed paper. The material used to form his smooth-walled fracture was glass. The strips divided the entire fracture into 10 to 20 mini parallel fractures with 2mm-3mm width. Romm found a linear relationship between the relative permeability and

saturation, $S_w = k_{rw}$, $S_{nw} = k_{rnw}$ such that $k_{rw}+k_{rnw} = 1$ which represents the X-curve behavior (Figure 1.1).

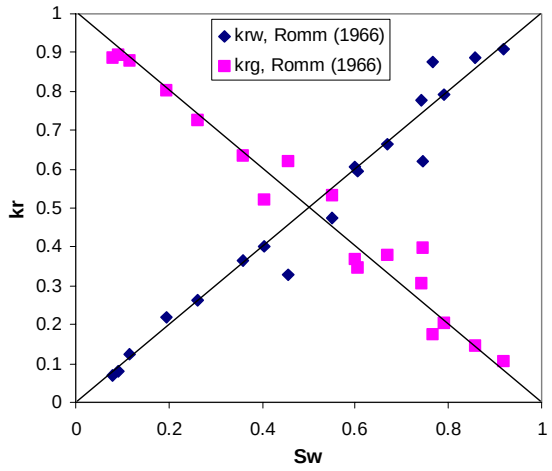

Figure 1.1: Romm's (1966) kerosene-water relative permeability in a smooth-walled fracture with strips of polyethylene or waxed paper.

Persoff et al. (1991) did experiments on gas and water flow through rough-walled fractures using transparent casts of natural fractured rocks. The experiment showed strong phase interference similar to the flow in porous media. In the experiments of both Persoff et al. (1991) and Persoff and Pruess (1995), flow of a phase was characterized by having a localized continuous flow path that is undergoing blocking and unblocking by the other phase. Diomampo (2001) performed experiments of nitrogen and water flow through smooth-walled artificial fractures. The relative permeability data of these published results are compared in Figure 1.2 against commonly used relative permeability relations for porous media, the Corey curve, and the viscous coupling model for fracture media suggested by Fourar and Lenormand (1998).

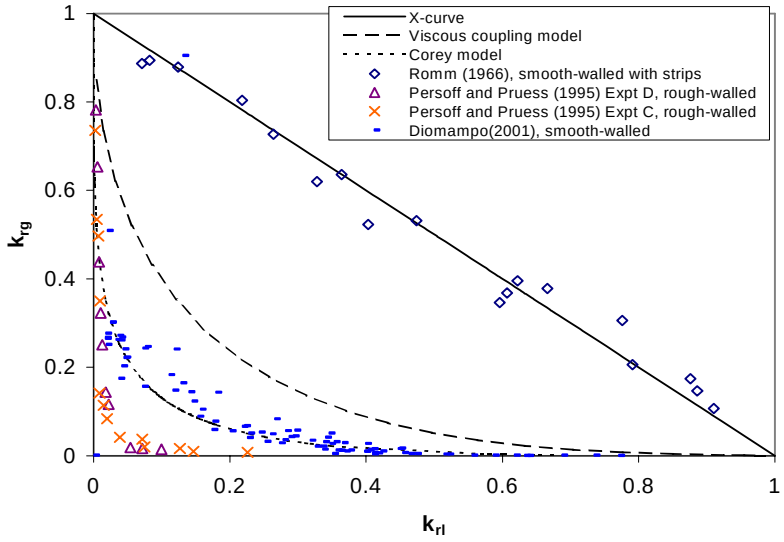

Figure 1.2: Compendium of previous measurements of relative permeabilities in fractures (Romm (1966) was conducted by kerosene-water flow, the rest were air-water flow).

It is obvious that these previous studies show a diversity of behavior of air-water relative permeabilities in fractures. However, the X-curve is commonly used in fractured reservoir simulation, which shows a contradiction with some previous measurements other than Romm's (1966). Presently, the flow mechanism and the characteristic behavior of relative permeability in fractures are still not well determined. The relationship between flow patterns and relative permeabilities in fractures is still not well studied. Through this research, we will visualize the two-phase flow behavior in fractures, obtain gas-water relative permeability from experiments, discuss how the shape of channels formed by phases affect the relative permeability, and finally propose a channel-oriented model for the relative permeability in fractures.

1.2 EXPERIMENTAL METHODOLOGY

Through this study, two nitrogen-water flow experiments were conducted at different environment temperature. The room temperature experiment was conducted at 24°C, while the high temperature experiment was at 90°C. The whole experiment system is illustrated in Figure 1.3, which shows the fluid supply, the fracture apparatus, back-pressure device, data acquisition system, and digital image recording.

Fracture Apparatus Description: The fracture is created by a smooth glass plate on top of an aluminum plate, confined by a metal frame bolted to the bottom plate. The aperture of the fracture in this research was set to 0.13mm by installing stainless shims in the fracture boundaries. Details of the fracture design were described in Diomampo (2001) and Chen et al. (2002). The schematic diagram and photograph of the fracture apparatus are shown in Figure 1.4. In the experiments, four pressure ports were drilled along the fracture for the overall and intermediate pressure difference measurements to minimize capillary end effect and to facilitate the absolute pressure measurement through the fracture.

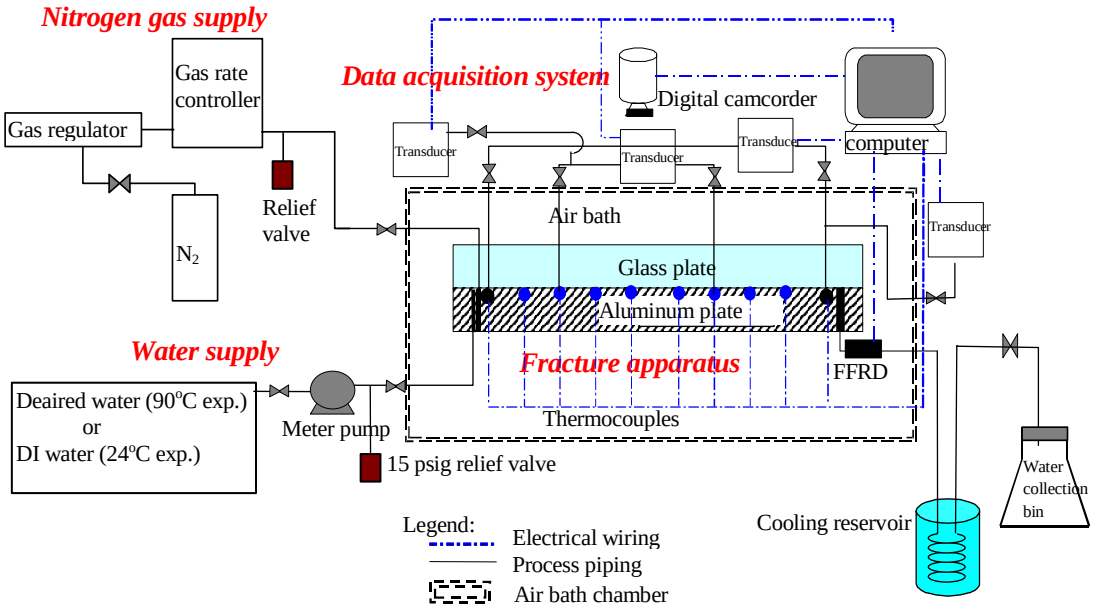

Figure 1.3: Process flow diagram for air-water experiment.

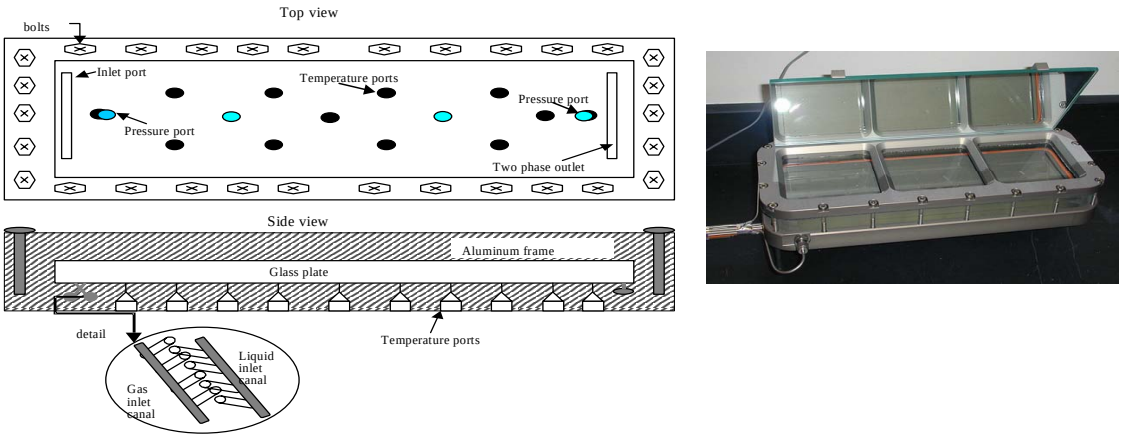

Figure 1.4: Schematic diagram and picture of fracture apparatus.

Fractional Flow Ratio Detector (FFRD): To obtain the instantaneous outlet flow rates and evaluate the evaporation effect at high temperature experiment, a fractional flow ratio detector (FFRD) was designed and constructed as shown in Figure 1.5. For the instantaneous gas rate measurement, the fractional flow ratio detector (FFRD) was used to measure the outlet gas and water fractional flow ratio, f_g and f_w.

$$f_g = \frac{q_{out,g}}{q_{out,t}} \text{ and } f_w = \frac{q_{out,w}}{q_{out,t}} \tag{1.12}$$

$$q_{out,t} = q_{out,w} + q_{out,g} \tag{1.13}$$

where $q_{out,g}$ is the output gas flow rate, $q_{out,w}$ is the output water flow rate, and $q_{out,t}$ is the output total flow rate. Once f_g and f_w are obtained in the steady-state condition, it is easy to evaluate $q_{out,g}$ by assuming that water rate remains constant from inlet to outlet of the fracture. This assumption can hold true if the wetting phase, water, flows in a continuous channel, and the water viscosity is much larger than the nonwetting phase. The principle of the FFRD is that different phases will have different refractive indices. A phototransistor (NTE 3038, NPN-Si, Visible) was installed inside the FFRD, producing different voltages when sensing different strengths of light. The water phase produces a higher voltage when flowing through the FFRD. Once the gas and water responses are obtained from the FFRD, the gas and water phase flow ratios are obtained by determining the ratio of the number of gas and water signals. Once the outlet gas and water fractional flow ratio, f_s and f_w, are obtained, it is easy to evaluate $q_{out,g}$ and $q_{out,w}$ by using the mass balance theory and the steam table if a steady-state condition is reached. The calibration of the FFRD is shown in Figure 1.6. The detail of this device can be found in Chen et al. (2002).

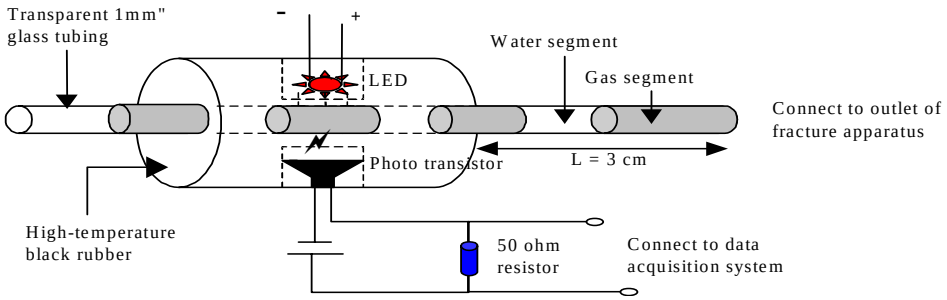

Figure 1.5: Schematic of fractional flow ratio detector (FFRD).

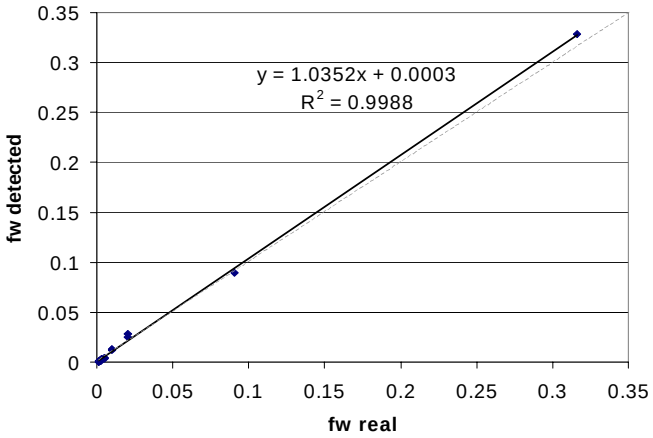

Figure 1.6:FFRD calibration (FFRD tubing ID: 1.0mm).

Saturation: Still images were extracted from digital video recorded during the experiments. The photographs were processed in a Matlab® program. The program does quadratic discriminant analysis (QDA) to group the pixels of the picture into three groups: the water phase, gas phase and the frame. The grouping is based on color differences. Saturation is calculated as total pixels of the liquid group over the sum of the gas and liquid groups. Figure 1.7 is a comparison of the gray-scaled image produced by the QDA program and the original photograph from the digital camcorder. The detail of this technique was described in Diomampo (2001) and in Chen et al. (2002).

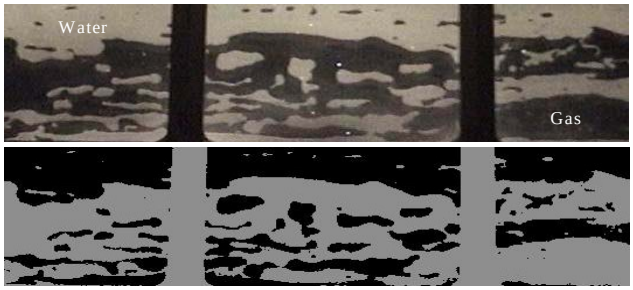

Figure 1.7: Comparison between the true color image of the fracture flow and gray scale image from Matlab QDA program used in measuring saturation.

Each experiment contains several runs with designated input rates of gas and water. Instantaneous output rates of gas and water were also measured by the FFRD device for the relative permeability calculation and flow rate comparison. Digital video was taken in each run when the flow reached steady state or repeated similar fluctuating behaviors. The

continuous images of each run were extracted from the video each 0.3 second. These hundreds of images in each run were then input to the computer programs for the saturation calculation, flow patterns recognition and characterization of the stability of the two-phase flow. The methodology used to integrate all the data and signals and then calculate the air-water relative permeabilities is illustrated in the flow chart in Figure 1.8. The detail of the data acquisition and analysis was described in Chen et al. (2002).

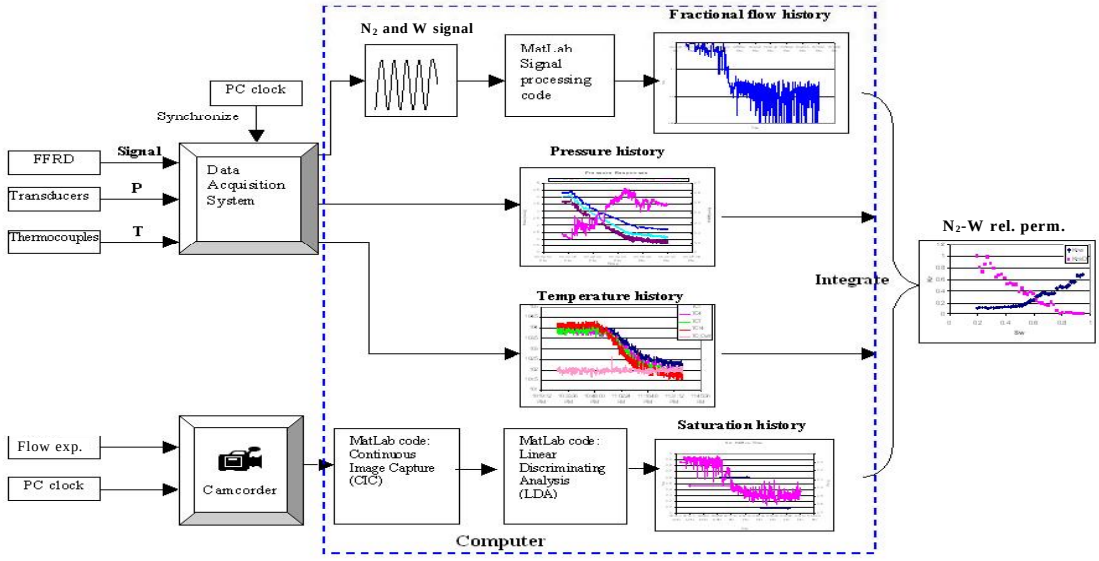

Figure 1.8: Data and signal processing flowchart.

1.3 EXPERIMENTAL RESULTS

Steady-state nitrogen-water relative permeability experiments were conducted at 24°C and 90°C. Before the experiment, the absolute permeability of the smooth-walled fracture was measured from the single-phase water flow. As can be seen in Figure 1.9, with the 0.13mm fracture aperture, the average permeability of the fracture measured is 1505 and 1387 darcies for 24°C and 90°C respectively. While applying the cubic law from Eq. 1.6, the permeability estimated is 1408 darcies. This is close to measurement values.

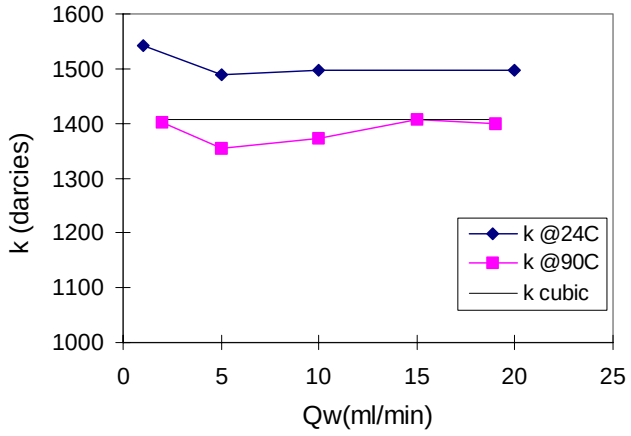

Figure 1.9: Absolute permeability of the fracture (aperture = 0.13mm) at 24°C and 90°C with different liquid rates.

1.3.1 Flow Pattern Classification

The transparent top glass of the fracture enabled us to observe and videotape the two phase flow behavior. The recorded digital video was then transformed to continuous snapshots with the frequency of 3 images/sec. More than 3000 still images were extracted from the digital video and used for the flow pattern characterization and saturation calculation in each experiment. By changing the flow rate for each phase, several evident flow patterns were observed. They are bubble flow, slug flow and channel flow in the descending order of water saturation, as shown in Figure 1.10.

The bubble flow could be seen only in extremely high water saturation. Due to the small fracture aperture (0.13mm), large gas bubbles propagated either in bullet-like or ellipse-like forms with longer longitudinal length. As the gas rate increased or water rate decreased, gas moved in narrow slugs and flowed discontinuously because of the relatively low gas flow rate. The higher pressure drop occurred mostly when a slug tried to break through the water region. Once the slug reached the outlet of the fracture, the pressure drop decreased. This type of slug movement was seen frequently in high water saturation situations. With the appearance of bubbles and slugs, the two-phase flow was fairly unstable. When the longitudinal size of slugs increased as the gas rate increased, the moving slugs intended to build stable gas channels to reach a stable condition. However, the attempt failed either because water broke the thinnest throat of the short-lived channel or because of the insufficient gas supply. This caused fluctuations in the water saturation, fractional flow and pressure drop.

As the gas rate increased further, the short-lived channel became more and more stable. The gas channel meandered through the fracture with branches and junctions because the viscous force was insufficient to break through intermediate water islands. We defined this kind of channel as tortuous channels as shown in Figure 1.10. The lifetime of these channels seemed to depend on the complexity and meander of their structure. Some tortuous channels might exist merely for a few seconds, whereas others existed for a long periods. The water saturation, water fractional flow and pressure drop histories plotted in Figure 1.11 are obtained from a tortuous-channel-dominated run where the water rate is 10 ml/min and gas rate is 50 ml/min . Clearly, even though constant gas and water rates were input to the fracture, the water saturation kept fluctuating in the fracture and the instantaneous f_w sensed from the FFRD followed this saturation fluctuation as shown in the top plot of Figure 1.11. The corresponding pressure response was also recorded as shown in the bottom plot of Figure 1.11. Most of the peaks in these two plots are due to the collapse, reconstruction and reconfiguration of channels, and some intrusions from other minor flow patterns (bubbles and slugs). It is also observed that the more tortuous the channel, the larger the pressure difference along the fracture.

On the other hand, the straight channel flow which was seen more frequently in high temperature or high gas fractional flow situations is shown in the bottom photograph of Figure 1.10. In this situation, almost all of the gas flows solely in the center region of the fracture, while most of the water flows above and below the gas path. Except for a small amount of immobile water inside the central gas channel, the gas path is more uniform and

is not tortuous in comparison with the tortuous channel flow. According to our observation, three major factors may affect the morphology of gas channels. They are the fractional flow of gas (viscous force), gas-water viscosity ratio (viscous force) and the interfacial tension (capillary force). Therefore for the same water saturation, the high-temperature case had straighter channels than the room-temperature case since the interfacial tension and water viscosity decrease as the temperature increases.

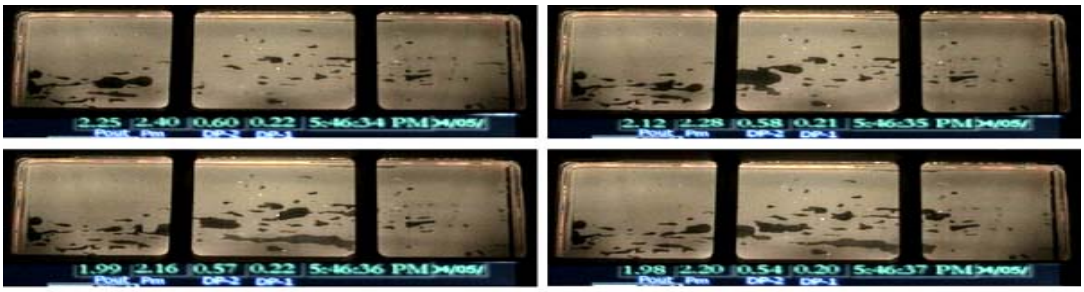

Bubble Flow

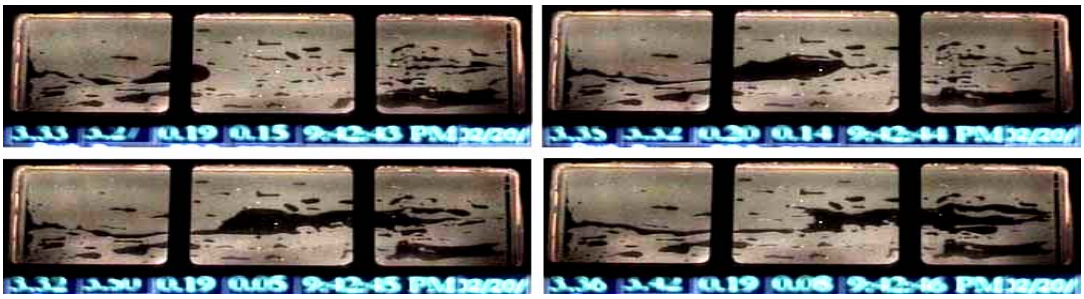

Slug Flow

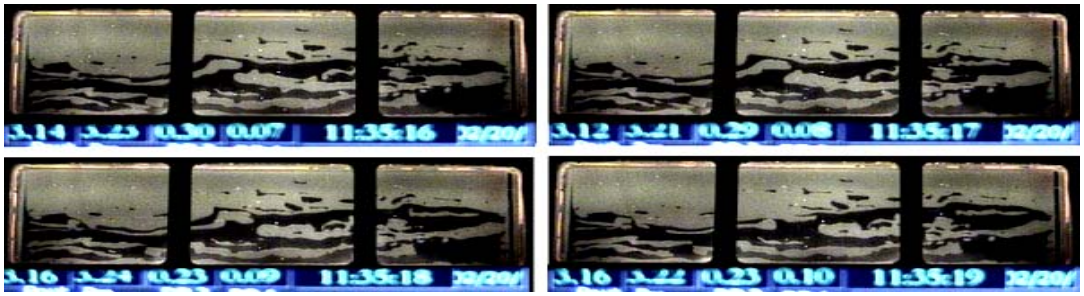

Tortuous Channel Flow

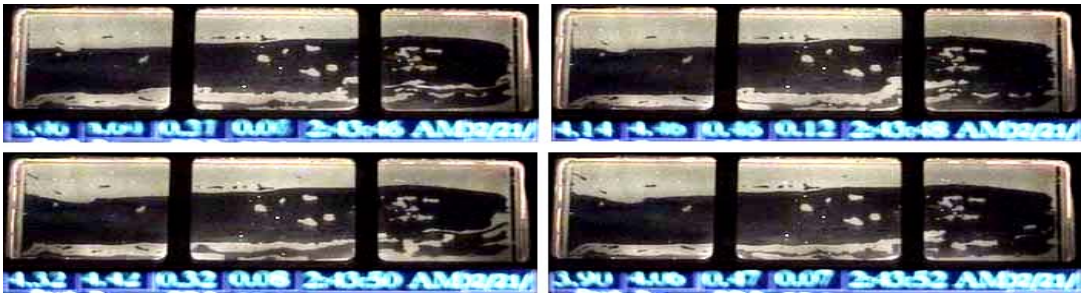

Straight Channel Flow

Figure 1.10: Photographs of flow patterns in the smooth-walled fracture. Each set contains four continuous images. Flow direction was from left to right.

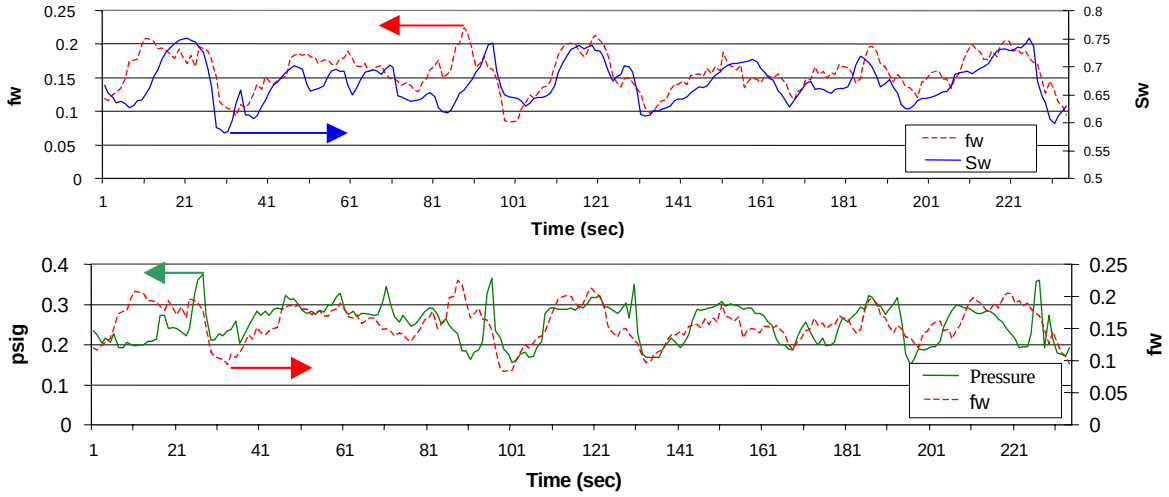

Figure 1.11: Relationship among water saturation, water fractional flow and pressure difference along the fracture at rates of Qw=10ml/min, Qg=50ml/min.

Figure 1.12 and 1.13 show flow pattern maps for nitrogen-water flow experiments at 24°C and 90°C respectively. The corresponding water saturation (approximate) is also provided in the figures. From these two figures, it is easy to find that the channel flow spans most of the water saturation range and major bubble and slug flows only exist in high water saturation situations. The shadow areas in the flow maps indicate transitional flow which means the flow pattern is a combination of the two neighboring distinct patterns. The transition between the slug flow and channel flow is defined as unstable channel flow. In this region, some large fingering slugs were able to bridge the two ends of the fracture. However, the bridged slug collapsed in a short time due to its unstable structure, water intrusion and the insufficient gas supply. By comparing Figure 1.13 with Figure 1.12, when the environment temperature increases, the channel flow region extends leftward due to the lower water viscosity and interfacial tension or capillary pressure. Both flow pattern maps have similar behavior to the flow map (glass fracture) presented by Fourar and Boris (1995).

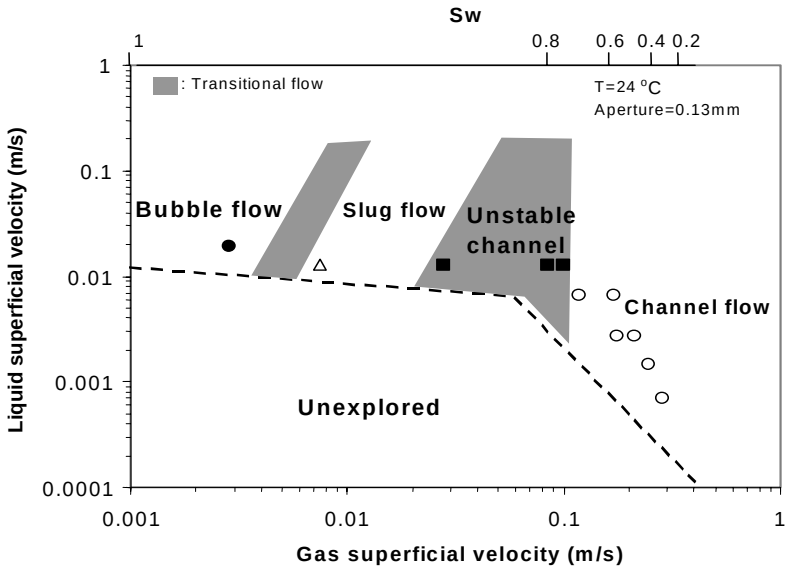

Figure 1.12: Flow pattern map for nitrogen-water flow in the smooth-walled fracture at 24°C.

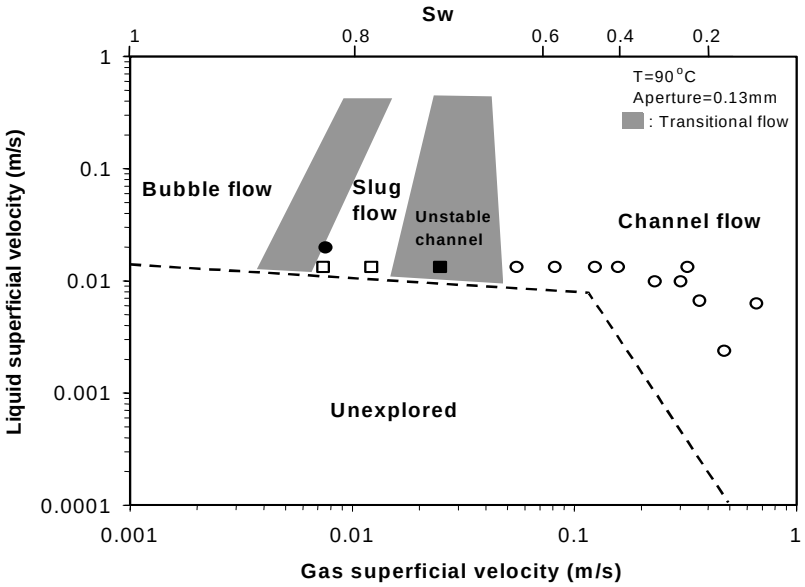

Figure 1.13: Flow pattern map for nitrogen-water flow in the smooth-walled fracture at 90°C.

1.3.2 Nitrogen-Water Relative Permeabilities

The nitrogen-water relative permeability was calculated by using Eq. 1.2 and Eq. 1.5 at 1 second frequency in each run. The instantaneous flow rate was obtained from the FFRD. In the high-temperature experiment, an evaporation effect from the water phase occurred due to the high temperature (90°C) and low operation pressure (less than 5 psi). Therefore, there was not only pure nitrogen but also some water vapor in the gas phase. It is important to evaluate the magnitude of the evaporation and hence correct parameters such as gas flow rate, contributed to by water vapor. The instantaneous fractional flow of water, f_w, obtained from the FFRD can be used to calculate evaporation rate, X, given input water and gas (nitrogen) rates. By using the mass balance theory and steam tables, X can be calculated by Eq. 1.14:

$$X = \frac{Q_{w0,l} - f_w(Q_{w0,l} + Q_{N2,g})}{1 + f_w(\frac{v_{w,g}}{v_{w,l}}) - f_w} \tag{1.14}$$

where, $Q_{w0,l}$ and $Q_{N2,g}$ are the input liquid water rate and gas rate respectively; $v_{w,l}$ and $v_{w,g}$ are the specific volume for water and steam (or water vapor) at some specific temperature; f_w is the instantaneous water fractional flow measured by the FFRD. Figure 1.14 shows the gas fractional flow, f_g, versus the steam ratio which is the volume of the steam evaporated from the water phase to the total volume of gas (sum of the input gas and produced steam). It is clear that water can evaporate to the vapor phase in the nitrogen-water experiment at 90°C, especially in a high gas rate situation. As shown in Figure 1.14, when gas fractional flow, f_g, is close to 1, the steam ratio reaches 0.73.

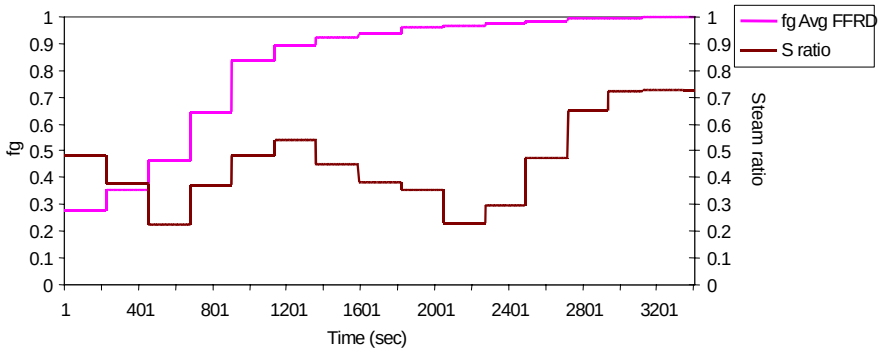

Figure 1.14: Steam ratios versus gas fraction flow in the nitrogen-water experiment at 90^{o}C.

The amount of water vapor that contributed the gas phase, $Q_{w,g}$, could be obtained from Eq. 1.15. The output gas rate, $Q_{g,out}$, then could be calculate by Eq. 1.16. The difference between input and output rates is shown in Figure 1.15. When the water fractional flow reaches 0.001, the gas rate increases four times. Because of the inconsistency of the input and output gas rates, one representative rate had to be used for calculating the gas velocity in Eq. 1.5. Since the saturation was calculated along the whole fracture, the mean of the input and output gas rates was used for the relative permeability calculation (Eq. 1.17).

$$Q_{w,g} = X \frac{v_{w,g}}{v_{w,l}} \tag{1.15}$$

$$Q_{g,out} = Q_{N2,g} + Q_{w,g} \tag{1.16}$$

$$\overline{Q}_g = \frac{Q_{N2,g} + Q_{g,out}}{2} \tag{1.17}$$

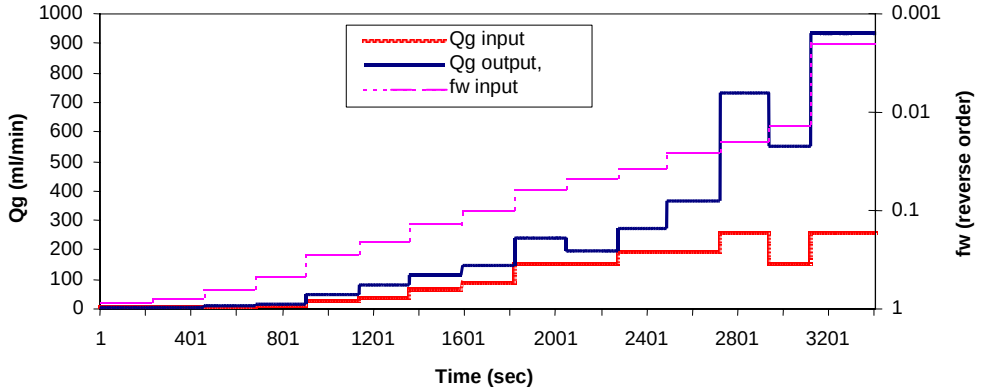

Figure 1.15: Input and output gas rates versus water fraction flow in the nitrogen-water experiment at 90^{o}C

Similar to the gas rate, the gas viscosity used in Eq. 1.5 had to be the mixture-gas viscosity instead of the pure nitrogen viscosity in the high-temperature case. The viscosity of the mixture of nitrogen and water vapor can be expressed as:

$$\mu_{mix,g} = \frac{\mu_{N2,g} Q_{N2,g} + \mu_{w,g} Q_{w,g}}{Q_{N2,g} + Q_{w,g}} \tag{1.18}$$

where, $\mu_{N2,g}$ and $\mu_{w,g}$ are the nitrogen viscosity and water vapor viscosity respectively; $Q_{N2,g}$ and $Q_{w,g}$ are the nitrogen volumetric rates and water vapor volumetric rates which was calculated from Eq. 1.15.

Comprehensive nitrogen-water relative permeabilities at room (24°C) and high temperature (90°C) are plotted and compared in Figure 1.16. Data points from room temperature and high temperature cases show acceptable correlation. In both cases, comprehensive water relative permeabilities are scattered under high water saturation owing to the slug and unstable-channel flows in the gas phase as shown in Figure 1.10. The vertically scattered effect in the gas relative permeabilities under extremely low water saturation may be associated with either the pressure fluctuation due to the slow moving water slugs or the difficulty in sensing the instantaneous f_w from the FFRD at low f_w. Overall, nitrogen-water relative permeability values at 90°C are greater than those at 24°C.

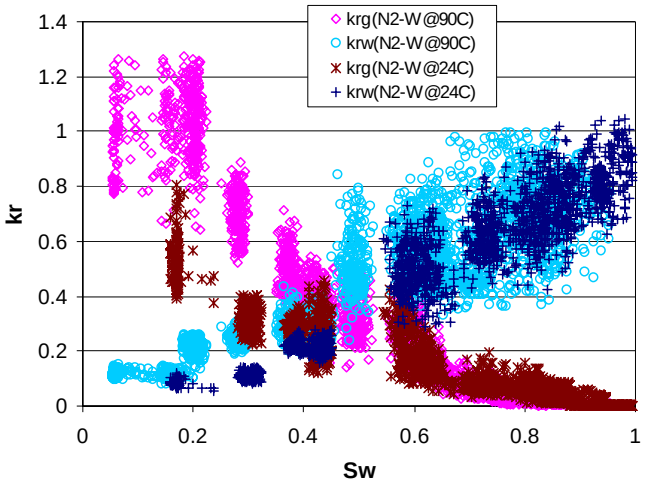

Figure 1.16: Comparison of comprehensive nitrogen-water relative permeabilities between 90°C and 24°C in the smooth-walled fracture.

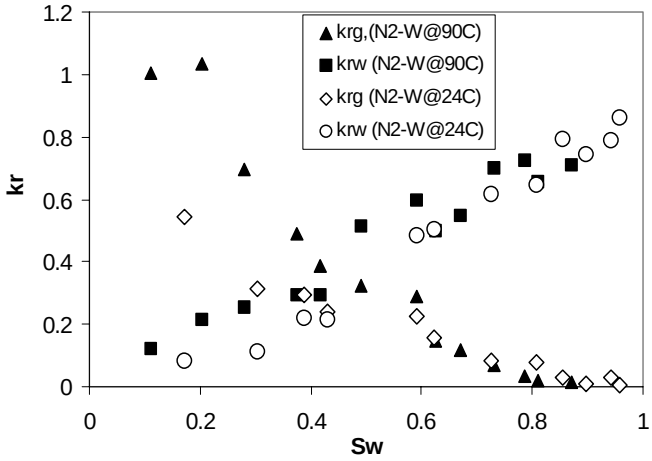

Figure 1.17: Comparison of average nitrogen-water relative permeabilities between 90°C and 24°C in the smooth-walled fracture.

By averaging through each run, Figure 1.17 shows averages of the full results shown in Figure 1.16. The water-phase relative permeability values at these two different temperatures are close and behave similar to the water part of the X-curve (linear line with slope=1). The gas-phase relative permeability values at these two different temperatures show different behaviors. It is evident that the gas curve at 90°C is higher than that at 24°C. This trend becomes more obvious as water saturation decreases. Essentially, average relative permeability curves at both 24°C and 90°C show less phase interference compared to the general relative permeability curves in porous media (Corey-type curves).

1.4 VALIDATION AND MODELING

1.4.1 Channel Morphology and Aspect

As shown in Figures 1.10, 1.12 and 1.13, the dominant flow pattern in the smooth-walled fracture is the channel flow. The morphology of the channels has an evident connection with phase rates, pressure difference and saturation. How does one characterize the morphology of phase channels and quantify the magnitude of "tortuosity" in phase channels? A channel tortuosity, τ_c, concept was created in this study to quantify the morphology of phase channels. The principal of this apparent parameter is based on the area of the channel and the smallest bounding rectangle that covers the whole channel. As shown in Figure 1.18, the binary images processed from continuous true-color images were input a Matlab® image-processing program, CAAR (Channel Area and Aspect Recognition), written during this project. This program will separate different flow patterns such as moving bubble, slugs, channels and residual islands. Phase channels were then isolated. The channel area, A_c (unit: pixel^2), length and width of the smallest bounding box, L_x and L_y (unit: pixel), were computed. The channel tortuosity was defined in Eq. 1.19.

$$\tau_c = \frac{L_x L_y}{A_c} \tag{1.19}$$

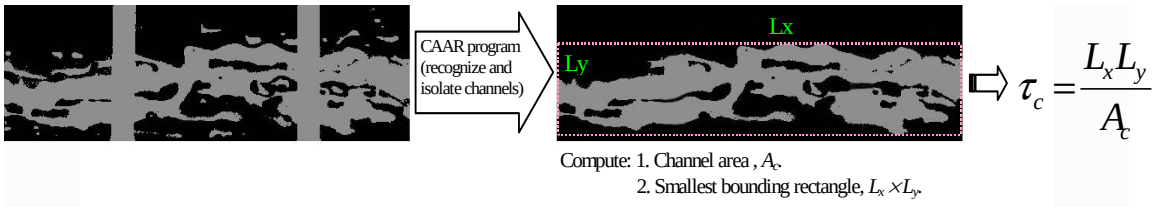

Figure 1.18: Evolution of channel tortuosity algorithm.

1.4.2 Channel-Oriented Modeling

Since the dominant flow pattern in this study is channel-like behavior, a channel-oriented model was proposed for modeling gas-water relative permeability. The concept of the channel-oriented model was based on the relationship between the fluid tortuosity and relative permeability. From the fundamentals of multiphase flow, the straight phase channel with a negligible thickness of wetting-phase film covering the top and bottom surface of the fracture will have the relative permeability close to the X-curve.

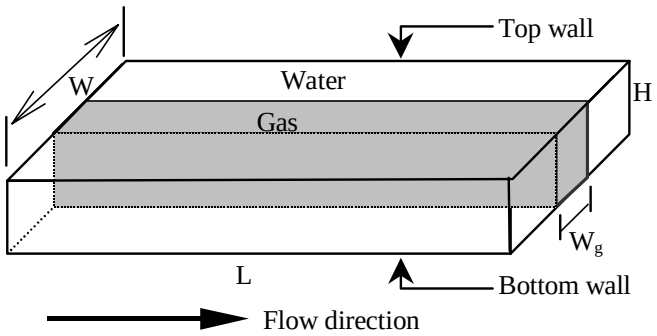

Figure 1.19: A simple model of a straight gas channel in a smooth-walled fracture.

By assuming negligible capillary pressure and gas slippage and gas inertia effect, the phase-flow equation can be derived from Poiseuille Equation. For gas phase:

$$Q_g = \frac{R_g^2 A_g}{8\mu_g}\frac{\Delta P_g}{L} \quad and \;\; A_g = W_g H\,,\; R_g = \frac{W_g H}{W_g + H} \tag{1.20}$$

According to Darcy's law for two-phase flow, we can rewrite Eq. 1.3 as:

$$Q_g = \frac{k_{abs} k_{rg} A}{\mu_g}\frac{\Delta P_g}{L} \tag{1.21}$$

where $A = WH$; the porosity (ϕ) and tortuosity (τ) are equal to 1 for the flow and fracture geometry shown in Figure 1.19. Therefore from the single-phase Darcy's law and Poiseuille equation, the absolute permeability is:

$$k_{abs} = \frac{\phi R^2}{8\tau} = \frac{R^2}{8} \tag{1.22}$$

Substituting Eq. 1.22 to Eq. 1.21 and equating Eq. 1.21 and Eq. 1.20, we obtain:

$$\frac{R_g^2 k_{rg} WH}{8\mu_g} = \frac{R_g^2 W_g H}{8\mu_g} \tag{1.23}$$

From Eq. 1.23, the gas-phase relative permeability is equal to the gas saturation:

$$k_{rg} = \frac{W_g}{W} = S_g \tag{1.24}$$

Similarly, for the water phase:

$$Q_w = \frac{R_w^2 A_w}{8\mu_w}\frac{\Delta P_w}{L} \quad and \;\; A_w = H(1 - W_g)\,,\; R_w = \frac{(1 - W_g)H}{1 - W_g + 2H} \tag{1.25}$$

From Eq. 1.2:

$$Q_w = \frac{k_{abs} k_{rw} A}{\mu_w}\frac{\Delta P_w}{L} \tag{1.26}$$

Equating Eq. 1.26 and 1.25, we can find that the water-phase relative permeability is equal to the water saturation:

$$k_{rw} = \frac{W - W_g}{W} = S_w \tag{1.27}$$

Consequently, in the absence of the capillary pressure and wetting-phase stratified flow on the top and bottom surface of the fracture, the straight phase-channel in the smooth-walled fracture will yield X-curve relative permeability as presented by Romm (1966). However, as shown in this study, the actual flow patterns in fractures seldom reach the ideal straight channel even though the fracture is smooth-walled. Most of the flow patterns are either fingering or tortuous channel instead, and relative permeabilities obtained from experiments show a deviation from X-curve as presented in Figure 1.17. As a result, a channel-oriented model to modify X-curve and take into account the channel tortuosity is created. In this model, we assume the channel tortuosity is directly proportional to the deviation of X-curve behavior. The relative permeability then can be modified to:

$$k_{rw} = \frac{S_w}{\tau_{c,w}} \tag{1.28}$$

$$k_{rg} = \frac{S_g}{\tau_{c,g}} \tag{1.29}$$

where $\tau_{c,w}$ and $\tau_{c,g}$ are the water channel tortuosity and gas channel tortuosity respectively. The image-processing program, CAAR, enabled us to input thousands of continuous images extracted from the video of the experiments with 0.3 second period and perform the flow-pattern recognition and then compute the tortuosity of gas and water channels. The computing algorithm is shown in Figure *1.18*. The mean tortuosity of gas and water channels was then computed by averaging all tortuosities in each run. Table 1.1 and 1.2 present the channel tortuosity in each run for room-temperature and high-temperature experiments. The channel weight means the percentage of the phase-channel area in the area of all flow patterns in that phase. This parameter can only be used as an indicator of the importance of channels' contribution to the saturation. We cannot relate this parameter to the importance of channels' contribution to the flow directly since the image can only express the flow behavior statically instead of dynamically. The phase tortuosity and channel weight versus the phase saturation is shown in Figures 1.20 to 1.23. It is evident that the higher the phase saturation, the less tortuous and more dominant that phase channel behaves. Generally speaking, the channels in the 90^{o}C case are less tortuous than in the 24^{o}C case. This shows consistency to most theoretical research.

Table 1.1: Channel-oriented parameters obtained from CAAR image processing program and comparison of experimental and modeling results for the nitrogen-water relative permeability at 24°C.

Rates (ml/min)	Saturation		Channel weight+		Average channel tortuosity		Experiment Results		Channel-oriented model		Viscous-coupling model		X-curve	
	Sw	Sg	Gas	Water	tao-g	tao-w	krg	krw	krg,C-O	krw,C-O	krg,V-C	krw,V-C	krg,X	krw,X
w15g2.2	0.957	0.043	0	1	NA*	1.038	0.002	0.863	NA	0.922	0.001	0.935	0.043	0.957
w10g20ii	0.941	0.059	0	0.999	NA	1.065	0.028	0.788	NA	0.884	0.002	0.911	0.059	0.941
w10g5	0.897	0.103	0.018	0.998	2.476	1.098	0.007	0.743	0.041	0.817	0.004	0.846	0.103	0.897
w10g20	0.854	0.146	0.001	0.991	2.6	1.143	0.03	0.794	0.056	0.747	0.007	0.783	0.146	0.854
w10g90	0.807	0.193	0.067	0.971	2.771	1.246	0.077	0.646	0.069	0.648	0.013	0.715	0.193	0.807
w10g120	0.726	0.274	0.377	0.973	2.797	1.61	0.086	0.619	0.098	0.451	0.028	0.6	0.274	0.726
w5g150	0.622	0.378	0.842	0.757	2.033	1.434	0.158	0.506	0.186	0.434	0.064	0.46	0.378	0.622
w5g200	0.592	0.408	0.971	0.806	1.699	1.437	0.225	0.487	0.24	0.412	0.078	0.422	0.408	0.592
w2g150	0.43	0.57	0.866	0.878	1.702	1.54	0.239	0.217	0.335	0.279	0.196	0.238	0.57	0.43
w2g200	0.387	0.613	0.855	0.75	1.746	1.639	0.294	0.221	0.351	0.236	0.241	0.196	0.613	0.387
w1g200	0.304	0.696	0.919	0.658	1.583	2.051	0.315	0.112	0.44	0.148	0.348	0.125	0.696	0.304
W0.5g200	0.171	0.829	0.99	0.062	1.337	2.464	0.541	0.083	0.62	0.069	0.577	0.041	0.829	0.171

* No channel detected.

\+ Channel weight = Area of phase channel / Area of that phase.

Table 1.2: Channel-oriented parameters obtained from CAAR image processing program and comparison of experimental and modeling results for the nitrogen-water relative permeability at 90°C.

Rates (ml/min)	Saturation		Channel weight		Average channel Tortuosity		Experiment Results		Channel-oriented model		Viscous-coupling model		X-curve model	
	Sw	Sg	Gas	Water	$\tau_{c,g}$	$\tau_{c,w}$	krg	krw	krg,C-O	krw,C-O	krg,V-C	krw,V-C	krg,X	krw,X
w15g2.2	0.87	0.13	0.0288	0.9982	3.5257	1.1393	0.0132	0.7115	0.0369	0.7637	0.0148	0.8062	0.13	0.87
w10g2.4	0.811	0.189	0.0862	0.9879	3.1016	1.2617	0.0193	0.6569	0.061	0.6426	0.0248	0.7194	0.189	0.811
w10g5	0.787	0.213	0.1828	0.9901	2.8263	1.3765	0.0361	0.7228	0.0753	0.5718	0.0297	0.6855	0.213	0.787
w10g10	0.731	0.269	0.2394	0.9743	2.7339	1.4912	0.0688	0.6994	0.0984	0.4902	0.0441	0.6063	0.269	0.731
w10g20	0.671	0.329	0.8164	0.8384	2.2601	1.5548	0.1161	0.5478	0.1455	0.4316	0.0645	0.5245	0.329	0.671
w10g30	0.625	0.375	0.8463	0.7831	2.1984	1.574	0.1493	0.5018	0.1706	0.397	0.0846	0.4637	0.375	0.625
w10g50	0.59	0.41	0.891	0.7515	1.9332	1.4471	0.2883	0.5978	0.2122	0.4076	0.1027	0.4192	0.41	0.59
w10g70	0.491	0.509	0.9628	0.7475	1.6662	1.5875	0.3233	0.5143	0.3053	0.3095	0.1688	0.3028	0.509	0.491
w7.5g120	0.417	0.583	0.9688	0.7	1.4871	1.5971	0.3887	0.294	0.3922	0.2609	0.2364	0.2243	0.583	0.417
w7.5g150	0.374	0.626	0.9745	0.6749	1.4565	1.5318	0.4898	0.2932	0.4298	0.2442	0.2828	0.1837	0.626	0.374
w5g150	0.281	0.719	0.9996	0.8896	1.1927	1.4993	0.6969	0.2527	0.6033	0.1871	0.4067	0.107	0.719	0.281
w5g200	0.202	0.798	0.9952	0.9635	1.1136	1.5373	1.0325	0.2153	0.7166	0.1314	0.5368	0.0571	0.798	0.202
w2g120	0.112	0.888	0.9954	0.99	1.1817	1.3	1.0052	0.1202	0.7514	0.0862	0.7187	0.0181	0.888	0.112

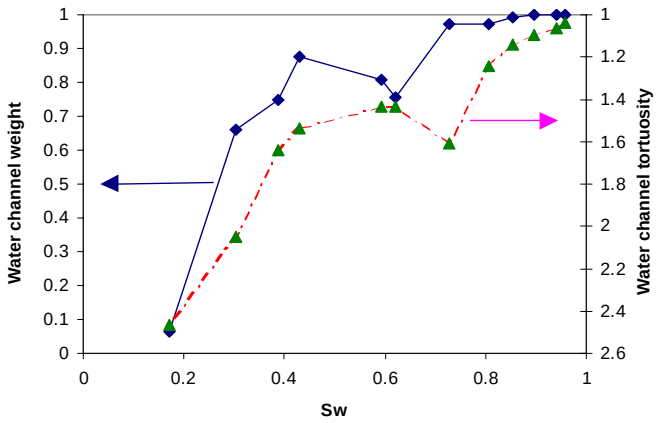

Figure 1.20: Water channel weight versus water channel tortuosity in the nitrogen-water experiment at 24^{o}C.

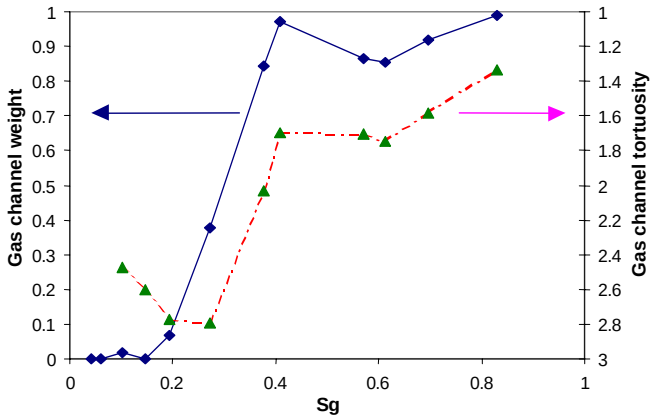

Figure 1.21: Gas channel weight versus gas channel tortuosity in the nitrogen-water experiment at 24^{o}C.

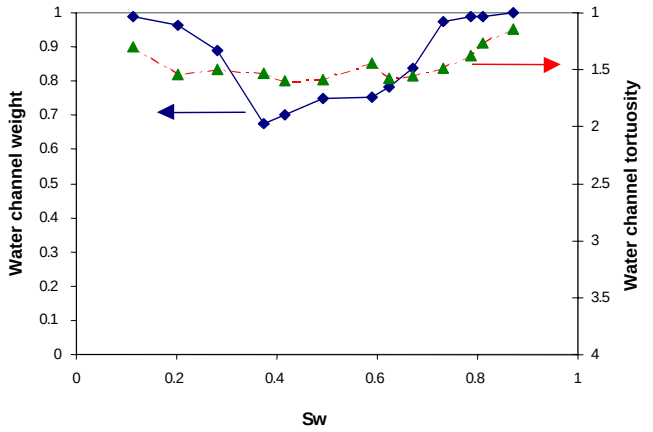

Figure 1.22: Water channel weight versus water channel tortuosity in the nitrogen-water experiment at 90^{o}C.

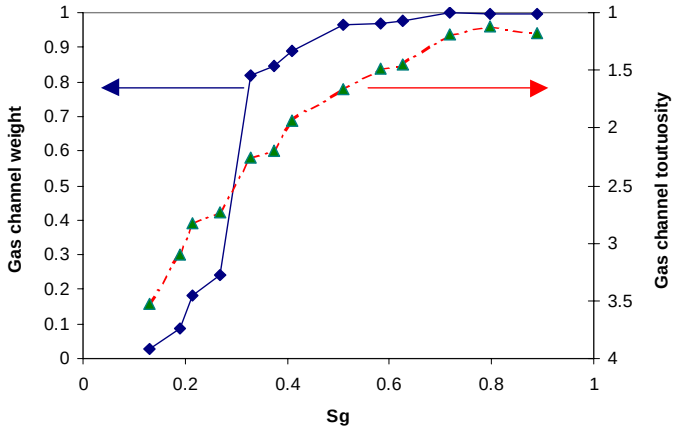

Figure 1.23: Gas channel weight versus gas channel tortuosity in the nitrogen-water experiment at 90°C.

The tortuosities in Table 1.1 and 1.2 were then used calculate k_{rw} and k_{rg} in Eq. 1.28 and 1.29. The results of channel-oriented model using experimental phase tortuosity for the nitrogen-water experiment at 24°C and 90 °C are plotted in Figures 1.24 and 1.25, respectively. The results from the channel-oriented model show good reproduction of the experimental results in both two cases, except near the endpoint of the gas-phase relative permeability in the 90°C case. As we can see in Figure 1.25, the experimental gas-phase relative permeability values near the endpoint are more than unity. This might be because considerable evaporation occurred in this range as shown previously in Figure 1.14. The mass contribution of the water vapor may lead to some measurement and calculation errors in the relative permeability. The discussion of the steam effect can be found in Chen et al. (2003).

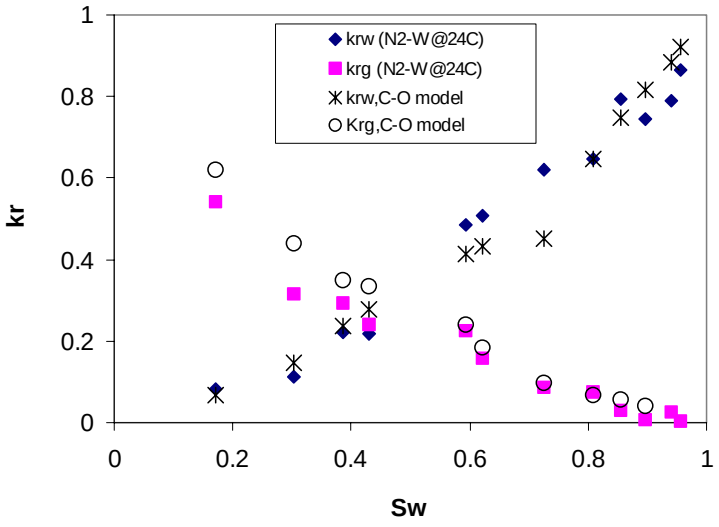

Figure 1.24: Validation of the channel-oriented model by using experimental phase tortuosity for the nitrogen-water experiment at 24°C.

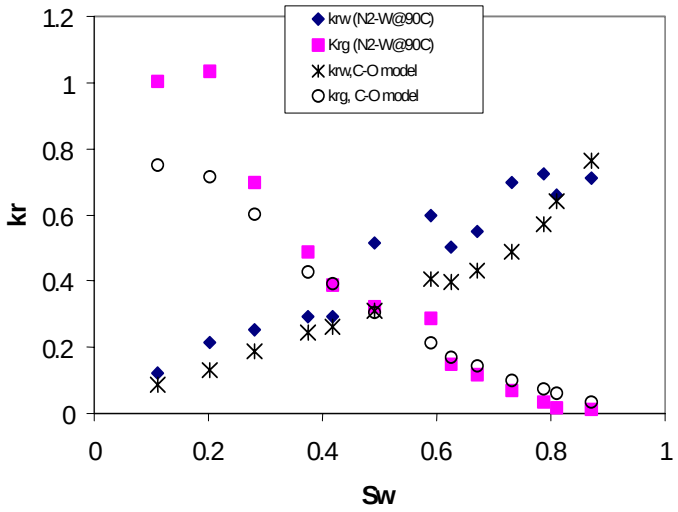

Figure 1.25: Validation of the channel-oriented model by using experimental phase tortuosity for the nitrogen-water experiment at 90°C.

1.4.3 Comparison with Models

Several relative permeability models have been suggested for modeling the relative permeability in fractures. Apart from the X-curve and Corey models mentioned previously, Fourar and Lenormand (1998) proposed an analytical viscous-coupling model for the relative permeability in fractures. This model was derived from Stoke's equation with the absence of fluid slippage and capillary pressure. The water (wetting) and gas (nonwetting) phase relative permeability in this model are:

$$k_{rw} = \frac{S_w^3}{2}(3 - S_w) \tag{1.30}$$

$$k_{rg} = (1 - S_w)^3 + \frac{3}{2}\frac{\mu_g}{\mu_w} S_w (1 - S_w)(2 - S_w) \tag{1.31}$$

It is clear that the water (wetting) phase relative permeability only depends on the saturation, while the gas (nonwetting) phase relative permeability is controlled by the viscosity ratio of the two fluids in this model.

The comparison of the channel-oriented model, viscous-coupling model and X-curve with the experimental relative permeability is shown in Figure 1.26 and 1.27 plotted from Table 1.1 and 1.2. The result from the Corey curve is not plotted here because its water-phase relative permeability shows a large inconsistency with the experimental result. The statistical analysis of the absolute errors between experimental and modeling relative permeabilities is presented in Table 1.3. In the 24°C experiment, both viscous-coupling model and channel-oriented model can represent the relative permeability with good accuracy, whereas both X-curve and Corey curve models show erratic results. In the 90°C experiment, the channel-oriented model has the best overall fit. Although the Corey curve can have a better fit for the gas-phase relative permeability, it cannot fit the water-phase relative permeability at all. To sum up, the proposed channel-oriented model can model

both relative permeabilities at room-temperature and high-temperature experiments successfully.

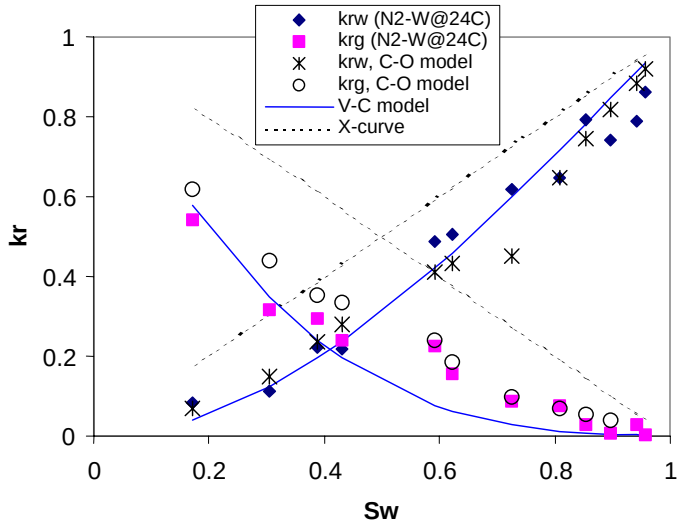

Figure 1.26: Comparison of the experimental relative permeability with the channel-oriented model, viscous-coupling model and X-curve for the nitrogen-water experiment at 24°C.

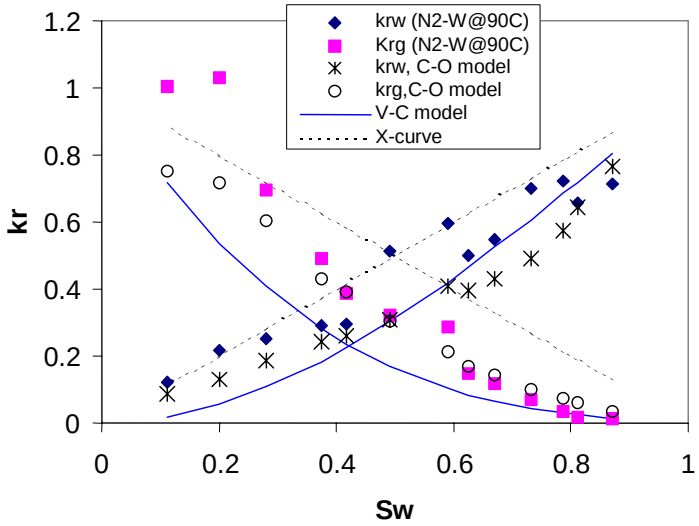

Figure 1.27: Comparison of the experimental relative permeability with the channel-oriented model, viscous-coupling model and X-curve for the nitrogen-water experiment at 90°C.

Table 1.3: Statistical analysis of the absolute errors between experimental and modeling relative permeabilities.

Models	24°C experiment					
	$\Sigma\lvert\Delta k_{rw}\rvert$	$\Sigma\lvert\Delta k_{rg}\rvert$	Mean($\lvert\Delta k_{rw}\rvert$)	Mean($\lvert\Delta k_{rg}\rvert$)	$\Sigma(\lvert\Delta k_{rw}\rvert+\lvert\Delta k_{rg}\rvert)$	Mean($\lvert\Delta k_{rw}\rvert+\lvert\Delta k_{rg}\rvert$)
X-curve	1.6098	2.3090	0.1341	0.1924	3.9188	0.1633
Corey curve (Corey, 1954)	2.7598	1.4239	0.2300	0.1187	4.1837	0.1743
Viscous-coupling model (Fourar and Lenormand, 1998)	0.6090	0.5810	0.0507	0.0484	1.1900	0.0496
Channel-oriented model (this work)	0.7194	0.4794	0.0599	0.0479	1.1988	0.0539

Models	90°C experiment					
	$\Sigma\lvert\Delta k_{rw}\rvert$	$\Sigma\lvert\Delta k_{rg}\rvert$	Mean($\lvert\Delta k_{rw}\rvert$)	Mean($\lvert\Delta k_{rg}\rvert$)	$\Sigma(\lvert\Delta k_{rw}\rvert+\lvert\Delta k_{rg}\rvert)$	Mean($\lvert\Delta k_{rw}\rvert+\lvert\Delta k_{rg}\rvert$)
X-curve	0.9387	2.1143	0.0722	0.1626	3.0531	0.1174
Corey curve (Corey, 1954)	4.2347	0.6448	0.3257	0.0496	4.8795	0.1877
Viscous-coupling model (Fourar and Lenormand, 1998)	1.3242	1.9263	0.1019	0.1482	3.2505	0.1250
Channel-oriented model (this work)	1.3081	1.0059	0.1006	0.0774	2.3140	0.0890

By reexamining Romm's (1966) experiment of kerosene-water flow in a smooth-walled fracture with strips of polyethylene or waxed water, we might propose the reason that his result follows X-curve behavior. In his work, strips of polyethylene or waxed water were deployed across the smooth-walled fracture as spacers. Therefore 20-30 parallel sub-fractures were generated from these strips. The width of these sub-fractures is only 2mm-3mm and the fracture length is 20 cm. With such a large aspect ratio, the phase-channel inside the sub-fracture was forced to be straight and the phase interference was almost one-dimensional, provided the main flow pattern in his kerosene-water flow experiment is channel flow. Therefore the channel tortuosity should be close to 1 in Romm's experiment. From the model we proposed in Eq. 1.28 and 1.29, the X-curve behavior was then completely expected.

1.5 CONCLUSION

1. In the results of nitrogen-water experiments, the water-phase relative permeability curves have the same behavior in both high-temperature and room-temperature cases, while the gas-phase curve at 90°C is higher than that at 24°C. The higher gas-phase curve at 90°C is due to the effects of the evaporated vapor.
2. The channel-oriented model can reproduce the experimental relative permeability results with good accuracy, whereas the viscous-coupling model can only fit the results at 24°C and both X-curve and Corey-curve model can only fit the experimental results partially.
3. From the observation of the flow pattern and the morphology of channels, we conclude that the two-phase relative permeability in fractures depends not only on the liquid type and fracture geometry but also on the two-phase flow patterns.
4. The proposed channel-oriented model can represent the relative permeability in the saturation range where the channel flow is the main or partial flow pattern. The representation of relative permeability in the extremely low and high water saturation range may be questionable because of the relative absence of phase channels.
5. The tortuosity of phase channels has to be obtained from the visualization of flow patterns. However, we are not able to see through the actual fracture rock in the real

world. Consequently, a mathematical expression of the tortuosity function is needed for the future modeling of the relative permeability in fractures.

2. UNIVERSAL CAPILLARY PRESSURE AND RELATIVE PERMEABILITY MODEL

This research project is being conducted by Senior Research Engineer Kewen Li and Professor Roland Horne. The objective of this project is to develop a general capillary pressure model using fractal geometry and to infer a relative permeability model from it.

2.1 SUMMARY

Capillary pressure is an important parameter in reservoir engineering. It is essential to represent capillary pressure curves mathematically in an appropriate way. The Brooks-Corey capillary pressure model has been accepted widely, however it has been found that the Brooks-Corey model can not represent capillary pressure curves of The Geysers rock samples. In fact, few existing models work for these rock samples. To this end, we modeled porous media using fractal geometry and derived a universal capillary pressure model theoretically. It was found that the universal capillary pressure model could be reduced to the frequently-used Brooks-Corey capillary pressure model when the fractal dimension of the porous media takes a limiting value. We also developed a relative permeability model from the universal capillary pressure model.

2.2 INTRODUCTION

Experimental data showed that the capillary pressure curves of rock samples with many fractures (The Geysers rock) were very different from those of rock samples without fractures (Berea sandstone). It was found that the Brooks-Corey (1964) capillary pressure model could be used to represent the curves of the rock without fractures but did not work for The Geysers rock samples with many fractures (Li and Horne, 2003). For example, Fig. 2.1 shows that the capillary pressure curve of Berea sandstone is a straight line on a log-log plot, which implies that the Brooks-Corey capillary pressure model works for Berea sandstone. However the capillary pressure curves of The Geysers rock are not straight lines, which demonstrates that the Brooks-Corey capillary pressure model does not work for The Geysers rock.

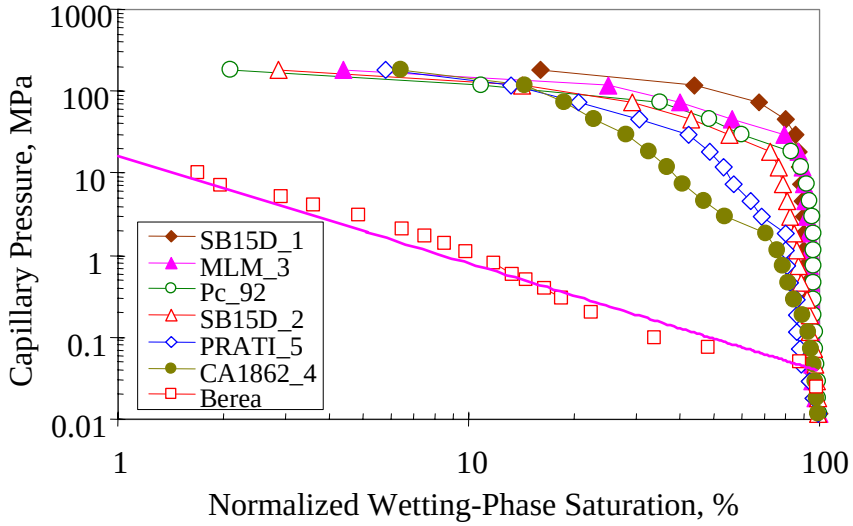

Figure 2.1: Capillary pressure curves of The Geysers rock and Berea sandstone.

Interestingly, fractal curves inferred from capillary pressure curves were good straight lines for all the rock samples, both those with and those without fractures, as shown in Fig. 2.2.

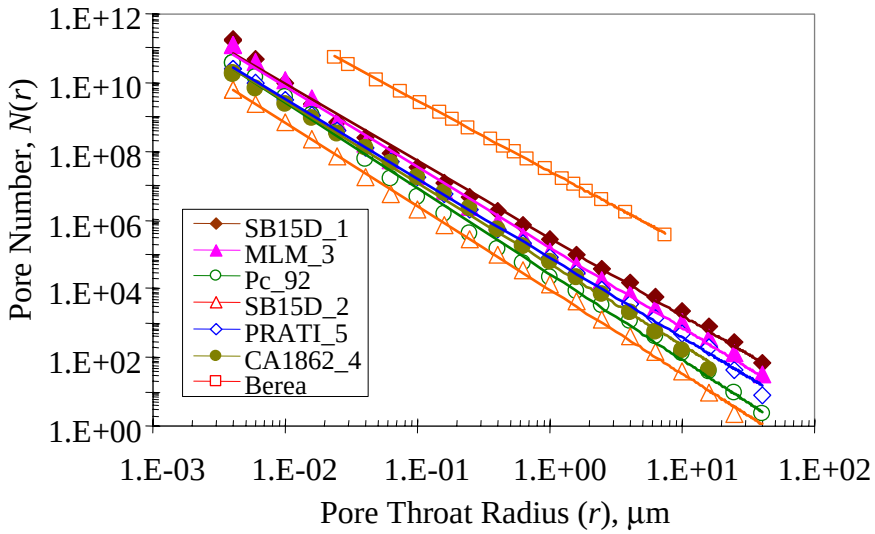

Figure 2.2: Relationships between N(r) and r of The Geysers rock and Berea sandstone.

This finding implies that a general capillary pressure model may exist to represent both the rock in which the Brooks-Corey model works and the rock in which the Brooks-Corey model does not work. In this study, such a general capillary pressure model was derived theoretically from fractal modeling. We also developed a general relative permeability model by substituting the universal capillary pressure model into the Purcell and the Burdine models.

2.3 THEORY

According to the basic concept of fractal geometry, the following expression applies to a fractal object:

$$N(r) \propto r^{-D_f} \tag{2.1}$$

where r is the radius (or characteristic length) of a unit chosen to fill the fractal object, $N(r)$ is the number of the units (with a radius of r) required to fill the entire fractal object, and D_f is the so-called fractal dimension. The fractal dimension is a representation of the heterogeneity of the fractal object. The greater the fractal dimension, the more heterogeneous the fractal object.

Capillary pressure curves measured by a mercury-intrusion technique are often used to infer the pore size distribution of rock samples. In making this inference, rock with solid skeleton and pores is represented by using a capillary tube model. $N(r)$ can be calculated

easily once capillary pressure curves measured using a mercury-intrusion technique are available. The unit chosen in this study was a cylindrical capillary tube with a radius of r and a length of l. So the volume of the unit is equal to $\pi r^2 l$ and $N(r)$ at a given radius of r is then calculated easily.

2.3.1 A universal capillary pressure model

Once $N(r)$ is known, the value of fractal dimension, D_f, can be determined from the relationship between $N(r)$ and r. The relationship between $N(r)$ and r should be linear on a log-log plot if the pore system of the rock is fractal.

According to the capillary tube model, $N(r)$ can be calculated as follows:

$$N(r) = \frac{V_{Hg}}{\pi r^2 l} \tag{2.2}$$

where l is the length of a capillary tube and V_{Hg} is the cumulative volume of mercury intruded in the rock sample when capillary pressure is measured.

Combining Eq. 2.1 and Eq. 2.2:

$$\frac{V_{Hg}}{\pi r^2 l} \propto r^{-D_f} \tag{2.3}$$

Arranging Eq. 2.3:

$$V_{Hg} \propto r^{2-D_f} \tag{2.4}$$

Considering a capillary tube model, capillary pressure can be calculated as follows:

$$P_c = \frac{2\sigma \cos\theta}{r} \tag{2.5}$$

where P_c is the capillary pressure, σ is the surface tension, and θ is the contact angle.

Substituting Eq. 2.5 into Eq. 2.4:

$$V_{Hg} \propto P_c^{-(2-D_f)} \tag{2.6}$$

The mercury saturation is calculated as follows:

$$S_{Hg} = \frac{V_{Hg}}{V_p} \tag{2.7}$$

where S_{Hg} is the mercury saturation and V_p is the pore volume of the core sample.

Substituting Eq. 2.7 into Eq. 2.6:

$$S_{Hg} = aP_c^{-(2-D_f)} \tag{2.8}$$

where a is a constant.

When V_{Hg} increases from 0 to 0^+, the corresponding capillary pressure increases from 0 to p_e. According to Eq. 2.8:

$$S_{Hg}(V_{Hg} \to 0) = \varepsilon = ap_e^{-(2-D_f)} \tag{2.9}$$

where ε is an infinite small positive value close to zero and p_e is the entry capillary pressure of the rock sample.

Similarly the capillary pressure reaches a maximum value (it can also be infinite) when V_{Hg} equals a maximum value. According to Eq. 2.8:

$$S_{Hg,\max} = aP_{c,\max}^{-(2-D_f)} \tag{2.10}$$

where $S_{Hg,\max}$ is the maximum mercury saturation and $P_{c,\max}$ is the maximum capillary pressure at $S_{Hg,\max}$.

Combining Eqs. 2.8, 2.9, and 2.10, we obtain:

$$\frac{S_{Hg} - \varepsilon}{S_{Hg,\max} - \varepsilon} = \frac{P_c^{-(2-D_f)} - p_e^{-(2-D_f)}}{P_{c,\max}^{-(2-D_f)} - p_e^{-(2-D_f)}} \tag{2.11}$$

Considering $\varepsilon \to 0$, Eq. 2.11 may be reduced to:

$$\frac{S_{Hg}}{S_{Hg,\max}} \approx \frac{P_c^{-(2-D_f)} - p_e^{-(2-D_f)}}{P_{c,\max}^{-(2-D_f)} - p_e^{-(2-D_f)}} \tag{2.12}$$

Using the wetting-phase saturation (the wetting-phase during mercury intrusion is air), Eq. 2.12 can be expressed as:

$$\frac{1-S_w}{1-S_{wr}} = \frac{P_c^{-(2-D_f)} - p_e^{-(2-D_f)}}{P_{c,\max}^{-(2-D_f)} - p_e^{-(2-D_f)}} \tag{2.13}$$

where S_w is the wetting-phase saturation and S_{wr} is the residual saturation of the wetting-phase.

Eq. 2.13 can be rearanged as:

$$\frac{1-S_w}{1-S_{wr}} = 1 - \frac{P_{c,\max}^{-(2-D_f)} - P_c^{-(2-D_f)}}{P_{c,\max}^{-(2-D_f)} - p_e^{-(2-D_f)}} \tag{2.14}$$

The normalized wetting-phase saturation is defined as:

$$S_w^* = \frac{S_w - S_{wr}}{1-S_{wr}} \tag{2.15}$$

Substituting Eq. 2.15 into Eq. 2.14:

$$S_w^* = \frac{P_{c,\max}^{-(2-D_f)} - P_c^{-(2-D_f)}}{P_{c,\max}^{-(2-D_f)} - p_e^{-(2-D_f)}} \tag{2.16}$$

Arranging Eq. 2.16:

$$P_c = [P_{c,\max}^{-\lambda} - (P_{c,\max}^{-\lambda} - p_e^{-\lambda})S_w^*]^{-\frac{1}{\lambda}} \tag{2.17}$$

where $\lambda = 2 - D_f$.

Eq. 2.17 can be reduced as follows:

$$P_c = P_{c,\max}(1 - bS_w^*)^{-\frac{1}{\lambda}} \tag{2.18}$$

where b is a constant and expressed as follows:

$$b = 1 - (\frac{p_e}{P_{c,\max}})^{-\lambda} \tag{2.19}$$

For D_f<2, if $P_{c,\max}$ approaches to infinite, then Eq. 2.18 can be reduced:

$$P_c = p_e (S_w^*)^{-\frac{1}{\lambda}} \tag{2.20a}$$

Eq. 2.20a is the frequently-used Brooks-Corey model, which was proposed empirically by Brooks and Corey.

According to the derivation in this report, one can see that the Brooks-Corey capillary pressure model has a solid theoretical basis. This may be why the Brooks-Corey model can be a good fit to capillary pressure curves of many rock samples.

In the case that b=1, Eq. 2.18 can be reduced to:

$$P_c = P_{c,\max} (1 - S_w^*)^{-\frac{1}{\lambda}} \tag{2.20b}$$

Eq. 2.20b is the imbibition capillary pressure model proposed by Li and Horne (2001) empirically (for D_f>2).

In the case that b=0, Eq. 2.18 can be reduced as:

$$P_c = P_{c,\max} \tag{2.20c}$$

Eq. 2.20c is a capillary pressure model for a single capillary tube.

One can see that Eq. 2.18, as a general capillary pressure model, could be applied in both complicated porous media and in a single capillary tube as well as in both drainage and imbibition cases.

Differentating Eq. 2.16:

$$\frac{dS_w^*}{dP_c} \propto -P_c^{-(3-D_f)} \tag{2.21}$$

Eq. 2.21 can also be expressed as:

$$\frac{dS_{Hg}}{dP_c} \propto P_c^{-(3-D_f)} \tag{2.22}$$

Eq. 2.22 is similar to the equation derived by Friesen and Mikula (1987):

$$\frac{dS_{Hg}}{dP_c} \propto P_c^{-(4-D_f)} \tag{2.23}$$

Note that we would obtain the same equation if a three-dimensional pore model, instead of a two-dimensional capillary tube model, is used to calculate the number of pore in porous media.

2.3.2 A new relative permeability model

There are two main ways to infer relative permeability from capillary pressure data. One is the Purcell approach (1949) and another is the Burdine approach (1953). We will derive new relative permeability models from the new capillary pressure model (Eq. 2.18) using both the Purcell and the Burdine approaches in this section.

Based on the Purcell model

Purcell developed an equation to compute rock permeability by using capillary pressure data. This equation can be extended readily to the calculation of multiphase relative permeability. In two-phase flow, the relative permeability of the wetting phase can be calculated as follows:

$$k_{rw} = \frac{\int_0^{S_w} dS_w/(P_c)^2}{\int_0^1 dS_w/(P_c)^2} \tag{2.24}$$

where k_{rw} and S_w are the relative permeability and saturation of the wetting phase; P_c is the capillary pressure as a function of S_w.

Similarly, the relative permeability of the nonwetting phase can be calculated as follows:

$$k_{rnw} = \frac{\int_{S_w}^1 dS_w/(P_c)^2}{\int_0^1 dS_w/(P_c)^2} \tag{2.25}$$

where k_{rnw} is the relative permeability of the nonwetting phase. It can be seen from Eqs. 2.24 and 2.25 that the sum of the wetting and nonwetting phase relative permeabilities at a specific saturation is equal to one. This may not be true in most porous media. In the next section, the relative permeabilities calculated using this method are compared to experimental data.

Substituting Eq. 2.18 into Eq. 2.24:

$$k_{rw} = \frac{\int_0^{S_w^*} [P_{c,\max}{}^{-\lambda} - (P_{c,\max}{}^{-\lambda} - p_e^{-\lambda}) S_w^*]^{\frac{2}{\lambda}} dS_w^*}{\int_0^1 [P_{c,\max}{}^{-\lambda} - (P_{c,\max}{}^{-\lambda} - p_e^{-\lambda}) S_w^*]^{\frac{2}{\lambda}} dS_w^*} \tag{2.26}$$

Defining:

$$S_{we} = P_{c,\max}{}^{-\lambda} - (P_{c,\max}{}^{-\lambda} - p_e^{-\lambda}) S_w^* \tag{2.27}$$

one can obtain:

$$dS_w^* = -\frac{1}{P_{c,\max}{}^{-\lambda} - p_e^{-\lambda}} dS_{we} \tag{2.28}$$

Substituting Eqs. 2.27 and 2.28 into Eq. 26:

$$k_{rw} = \frac{\int_\beta^{S_{we}} (S_{we})^{\frac{2}{\lambda}} dS_{we}}{\int_\beta^\alpha (S_{we})^{\frac{2}{\lambda}} dS_{we}} \tag{2.29}$$

where:

$$\beta = P_{c,\max}^{-\lambda} \tag{2.30}$$

$$\alpha = p_e^{-\lambda} \tag{2.31}$$

After integrating:

$$k_{rw} = \frac{(S_{we})^{\frac{2+\lambda}{\lambda}} - \beta^{\frac{2+\lambda}{\lambda}}}{\alpha^{\frac{2+\lambda}{\lambda}} - \beta^{\frac{2+\lambda}{\lambda}}} \tag{2.32}$$

Eq. 2.32 can be expressed as:

$$k_{rw} = \frac{[P_{c,\max}{}^{-\lambda} - (P_{c,\max}{}^{-\lambda} - p_e^{-\lambda}) S_w^*]^{\frac{2+\lambda}{\lambda}} - (P_{c,\max})^{-(2+\lambda)}}{(p_e)^{-(2+\lambda)} - (P_{c,\max})^{-(2+\lambda)}} \tag{2.33}$$

According to Eq. 2.25, the relative permeability of the nonwetting phase can be calculated as follows:

$$k_{rnw} = \frac{\alpha^{\frac{2+\lambda}{\lambda}} - (S_{we})^{\frac{2+\lambda}{\lambda}}}{\alpha^{\frac{2+\lambda}{\lambda}} - \beta^{\frac{2+\lambda}{\lambda}}} \tag{2.34}$$

Eq. 2.34 can be expressed as:

$$k_{rnw} = \frac{(P_e)^{-(2+\lambda)} - [P_{c,\max}{}^{-\lambda} - (P_{c,\max}{}^{-\lambda} - p_e^{-\lambda})S_w^*]^{\frac{2+\lambda}{\lambda}}}{(p_e)^{-(2+\lambda)} - (P_{c,\max})^{-(2+\lambda)}} \tag{2.35}$$

According to Eq. 2.33:

$$k_{rw}(S_w^* = 0) = 0 \tag{2.36}$$

and

$$k_{rw}(S_w^* = 1) = 1 \tag{2.37}$$

According to Eq. 2.35:

$$k_{rnw}(S_w^* = 0) = 1 \tag{2.38}$$

and

$$k_{rnw}(S_w^* = 1) = 0 \tag{2.39}$$

One can see from Eqs. 2.33 and 2.35 that relative permeability depends not only upon the heterogeneity (represented by fractal dimension through the parameter m) but also upon the pore size of porous media in some cases.

when D_f<2 and $P_{c,\max}$ approaches infinity, Eqs. 2.33 and 2.35 can be reduced to the simple Purcell relative permeability model expressed as follows:

$$k_{rw} = (S_w^*)^{\frac{2+\lambda}{\lambda}} \tag{2.40}$$

$$k_{rnw} = 1 - (S_w^*)^{\frac{2+\lambda}{\lambda}} \tag{2.41}$$

Therefore the new relativer permeability model (Eqs. 2.33 and 2.35) encompasses the Purcell relative permeability model (Eqs. 2.40 and 2.41).

In cases where $P_{c,\max}$ has a finite value, Eqs. 2.33 and 2.35 can be reduced as follows:

$$k_{rw} = \frac{(1 - bS_w^*)^m - 1}{(1-b)^m - 1} \tag{2.42}$$

$$k_{rnw} = \frac{(1-b)^m - (1 - bS_w^*)^m}{(1-b)^m - 1} \tag{2.43}$$

where b is defined in Eq. 2.19 and m is expressed as follows:

$$m = \frac{2+\lambda}{\lambda} = \frac{4 - D_f}{2 - D_f} \tag{2.44}$$

Note that m is a paramter associated with the heterogeneity of the porous media because the fractal dimension D_f is a representation of heterogeneity. Parameter b is associated with the size of the pore in porous media.

Based on the Burdine model

Burdine (1953) developed equations similar to Purcell's method by introducing a tortuosity factor as a function of wetting phase saturation. The relative permeability of the wetting phase can be computed as follows:

$$k_{rw} = (\lambda_{rw})^2 \frac{\int_0^{S_w} dS_w / (P_c)^2}{\int_0^1 dS_w / (P_c)^2} \tag{2.45}$$

where λ_{rw} is the tortuosity ratio of the wetting phase. According to Burdine, λ_{rw} could be calculated as follows:

$$\lambda_{rw} = \frac{\tau_w(1.0)}{\tau_w(S_w)} = \frac{S_w - S_m}{1 - S_m} \tag{2.46}$$

where S_m is the minimum wetting phase saturation from the capillary pressure curve; $\tau_w(1.0)$ and $\tau_w(S_w)$ are the tortuosities of the wetting phase when the wetting phase saturation is equal to 100% and S_w respectively.

In the same way, relative permeabilities of the nonwetting phase can be calculated by introducing a nonwetting phase tortuosity ratio. The equation can be expressed as follows:

$$k_{rnw} = (\lambda_{rnw})^2 \frac{\int_{S_w}^{1} dS_w / (P_c)^2}{\int_{0}^{1} dS_w / (P_c)^2} \tag{2.47}$$

where λ_{rnw} is the tortuosity ratio of the nonwetting phase, which can be calculated as follows:

$$\lambda_{rnw} = \frac{\tau_{nw}(1.0)}{\tau_{nw}(S_w)} = \frac{1 - S_w - S_e}{1 - S_m - S_e} \tag{2.48}$$

Here S_e is the equilibrium saturation of the nonwetting phase; τ_{nw} is the tortuosity of the nonwetting phase.

Using the similar procedure as deriving Eqs. 2.33 and 2.35, one can obtain:

$$k_{rw} = (S_w^*)^2 \frac{[P_{c,\max}{}^{-\lambda} - (P_{c,\max}{}^{-\lambda} - p_e^{-\lambda})S_w^*]^{\frac{2+\lambda}{\lambda}} - (P_{c,\max})^{-(2+\lambda)}}{(P_e)^{-(2+\lambda)} - (P_{c,\max})^{-(2+\lambda)}} \tag{2.49}$$

$$k_{rnw} = (1 - S_w^*)^2 \frac{(P_e)^{-(2+\lambda)} - [P_{c,\max}{}^{-\lambda} - (P_{c,\max}{}^{-\lambda} - p_e^{-\lambda})S_w^*]^{\frac{2+\lambda}{\lambda}}}{(P_e)^{-(2+\lambda)} - (P_{c,\max})^{-(2+\lambda)}} \tag{2.50}$$

when D_f<2 and $P_{c,\max}$ approaches infinity, Eqs. 2.49 and 2.50 can be reduced to the simple Brooks-Corey relative permeability model expressed as follows:

$$k_{rw} = (S_w^*)^{\frac{2+3\lambda}{\lambda}} \tag{2.51}$$

$$k_{rnw} = (1 - S_w^*)^2 [1 - (S_w^*)^{\frac{2+\lambda}{\lambda}}] \tag{2.52}$$

Therefore the new relative permeability model (Eqs. 2.49 and 2.50) encompasses the Brooks-Corey relative permeability model (Eqs. 2.51 and 2.52).

In the case in which $P_{c,\max}$ has a finite value, Eqs. 2.49 and 2.50 can be reduced as follows:

$$k_{rw} = \frac{(S_w^*)^2[(1-bS_w^*)^m - 1]}{(1-b)^m - 1} \tag{2.53}$$

$$k_{rnw} = \frac{(1-S_w^*)^2[(1-b)^m - (1-bS_w^*)^m]}{(1-b)^m - 1} \tag{2.54}$$

In the case in which b=1 and m>0, Eqs. 2.53 and 2.54 can be reduced as follows:

$$k_{rw} = (S_w^*)^2[1-(1-S_w^*)^m] \tag{2.55}$$

$$k_{rnw} = (1-S_w^*)^{2+m} \tag{2.56}$$

In the case in which m=0, Eqs. 2.55 and 2.57 can be reduced as follows:

$$k_{rw} = (S_w^*)^2 \tag{2.57}$$

$$k_{rnw} = (1-S_w^*)^2 \tag{2.58}$$

Eqs. 2.57 and 2.58 are the relative permeability model in a single capillary tube.

Eqs. 2.51 and 2.52 have been tested against experimental data in many cases. However the new relative permeability models developed in this study are yet to be verified.

2.4 RESULTS

Relative permeability curves were calculated according to the new model (see Eqs. 2.53 and 2.54) using different values of fractal dimension. The results are plotted in Fig. 2.3. One can see that the relative permeability curves of the nonwetting phase (represented by steam phase in Fig. 2.3) are almost the same for different values of fractal dimension. However, the relative permeability curves of the wetting phase (represented by water phase in Fig. 2.3) are different for different values of fractal dimension. The fractal dimension of The Geysers rock is greater than 2.3 (Li and Horne, 2003). Fig. 2.3 shows that the corresponding relative permeability curves have different features from those with fractal dimension less than 2.0, as predicted by the model (see Eqs. 2.53 and 2.54). One can see that the values of the water phase relative permeability for the fractal dimension over 2.3 are very small until the normalized water saturation reaches about 90%. This phenomino may be berified by future experimental data of steam and water relative permeability measured in The Geysers rock.

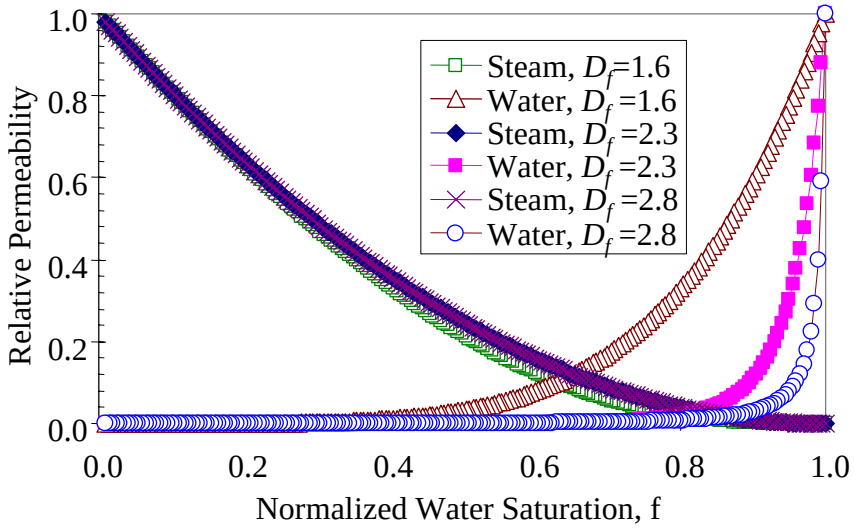

Figure 2.3: Typical relative permeability curves calculated using the new model with different values of fractal dimension.

2.5 CONCLUSIONS

Based on the present study, the following conclusions may be drawn:

1. A universal model has been developed to represent capillary pressure curves of porous media using fractal geometry.
2. Relative permeability models for both wetting-phase and nonwetting-phase have been developed accordingly.

3. CALCULATION OF STEAM AND WATER RELATIVE PERMEABILITIES AT THE GEYSERS AND SALTON SEA GEOTHERMAL RESERVOIRS USING PRODUCTION DATA

This project is being conducted by Research Assistant Jericho Reyes and Prof. Roland Horne. The goal of this research is to calculate the steam and water relative permeabilities at The Geysers and Salton Sea geothermal reservoirs from available production data. A method was developed to estimate the relative permeability curves using Darcy's Law from mass production rates of steam and water that is available from the DOGGR database. Results show The Geysers behavior approaches the X-curve behavior and Salton Sea behavior approaches Corey curve behavior.

3.1 INTRODUCTION

Recovery of energy from a geothermal reservoir requires that mass be withdrawn from it. Accurate knowledge of the ease in which mass can be produced, as well as other parameters involved in the recovery process is of substantial economic value in making most effective use of the resource.

There are two types of geothermal reservoirs: the vapor-dominated reservoir, where steam is the principal recovery fluid, and the liquid-dominated reservoir, where liquid water is the principal recovery fluid. In both cases, the interaction between these two different phases has been the subject of numerous studies. Most of the experimental activities encounter difficulty due to the phase changes during multiphase flow. An alternative way of determining how these two phases interact while in a state of flow would be very useful in the prediction of the ultimate recovery of the resource. Quantifying this interaction, by calculating the relative permeability of each of the phases, is of particular importance.

The objective of this study is to develop a method to calculate the relative permeability of steam and water by using production data from active geothermal fields.

Knowledge of the relative permeabilities of steam will provide better understanding of the fluid flow interactions in the geothermal reservoir, and this is valuable in estimating the performance of a geothermal field and its capacity for further exploitation.

3.2 BACKGROUND

There have been numerous attempts to characterize the steam and water relative permeability curves both experimentally and theoretically. The main difficulty of such undertakings has been the phase changes that occur in steam and water multiphase flow. A number of experiments have been made to measure steam-water relative permeabilities, such as in air-water (Diomampo, 2001) and water-oil. Current research on steam-water permeability in fractures (Chen et al. 2002), gives us a preliminary insight on the characteristics of the interaction of these two phases with one another.

The two most commonly used functions for relative permeability are the X-curve and the Corey-curve (Corey, 1954). These functions are dependent on phase saturation. The X-curve has a linear relationship with saturation:

$$k_{rl} = S_l \tag{3.1}$$

$$k_{rg} = S_g \tag{3.2}$$

where S_l and S_g are the liquid and gas saturation respectively. The Corey curves relate relative permeability to the irreducible or residual liquid and gas saturation, S_{rl} and S_{rg} :

$$k_{rl} = S^{*4} \tag{3.3}$$

$$k_{rg} = (1 - S^*)^2 (1 - S^{*2}) \tag{3.4}$$

$$S^* = (S_l - S_{rl}) / (1 - S_{rl} - S_{rg}) \tag{3.5}$$

Chen et al. (2002) developed a method to compare steam- and air-water transport through fractured media. The main finding was that steam-water flow behavior in fractures is different from that of nitrogen-water flow. Chen et al. (2002) found less phase interference in steam-water flow, and saw the behavior of the steam-water relative permeabilities behave closer to the X-curve.

The DOGGR Database was made available publicly by the California Division of Oil, Gas and Geothermal Resources. The database contains production histories of, among others, the Geysers and Salton Sea geothermal wells. The data include temperature, pressure and steam and water production rates, and these parameters were used here in this study. The Geysers Geothermal Field, a vapor-dominated reservoir field, is located in Northern California about 130 km north of San Francisco. The Salton Sea Geothermal Field, a liquid-dominated reservoir field, is located in Imperial County in Southern California.

3.3 METHOD

Shinohara (1978) developed a method to estimate the steam and water relative permeabilities in geothermal reservoirs. This method was applied to the Wairakei field in New Zealand. This method is very useful, in that it only needs the production flow rate history and the temperature of the reservoir, as well as the ability to evaluate each well separately.

Some of the assumptions of this method include:

(1) The pressure gradient is constant for a short time in each well.
(2) The product of permeability and flowing area is constant in each well.
(3) Fluid flow follows Darcy's Law.

Under these assumptions and from Darcy's law:

$$Q_w = \rho_w \frac{k}{\mu_w} k_{rw} Ap' \tag{3.6}$$

$$Q_s = \rho_s \frac{k}{\mu_s} k_{rs} Ap' \tag{3.7}$$

where Q is the mass flowrate, ρ is the density, μ is the dynamic viscosity, k_r is the relative permeability, k is the absolute permeability of the geothermal rock, A is the cross sectional area of flow, and p' is the pressure gradient. The subtitles w and s refer to water and steam respectively.

Dividing Equation 3.6 by Equation 3.7 gives us:

$$\frac{Q_w}{Q_s} = \frac{\upsilon_w}{\upsilon_s} \frac{k_{rw}}{k_{rs}} \tag{3.8}$$

where υ is the kinematic viscosity.

Taking the sum of Equations 3.6 and 3.7 gives us:

$$Q = Q_w + Q_s = \left(\rho_w \frac{k_{rw}}{\mu_w} + \rho_s \frac{k_{rs}}{\mu_s} \right) kAp' = \left(\frac{k_{rs}}{\upsilon_s} \right) \left[1 + \left(\frac{Q_w}{Q_s} \right) \right] kAp' \tag{3.9}$$

where Q is the total of mass production rate of steam and water.

If we assume kAp' is constant in each well, then Equation 3.9 shows that a plot of Q vs Q_w/Q_s would be almost linear, and we can find the value of kAp' from either the intercept or the gradient of the line on the graph. This intercept, where $Q_w/Q_s = 0$, becomes Q^*, where:

$$Q^* = \frac{1}{\upsilon_s} kAp' \tag{3.10}$$

Because $k_{rs} = 1$ at $Q_w = 0$, then, substituting Equation 3.10 into Equation 3.6 and 3.7,

$$k_{rw} = \left(\frac{\upsilon_w}{\upsilon_s} \right) \left(\frac{Q_w}{Q^*} \right) \tag{3.11}$$

and

$$k_{rs} = \frac{Q_s}{Q^*} \tag{3.12}$$

Therefore, knowing Q^* , we can calculate k_{rs} and k_{rw}, by also knowing Q_w, Q_s, υ_s, and υ_w.

Water saturation can be calculated from

$$S_w = \frac{(1-x)\nu_w}{(1-x)\nu_w + x\nu_w} \tag{3.13}$$

where x is the mass fraction of steam and v_w and v_s is the specific volume of water and steam, respectively.

In choosing the wells to use in this study, a couple of issues had to be addressed. First, for the vapor-dominated reservoir, we had to find data that had both steam and water production in order to calculate multiphase properties. Of the 503 wells made available to us from The Geysers, 25 of these wells produced water. Nine wells were ultimately used, as these wells had a sufficient number of readings for the calculation.

Also, the first assumption of Shinohara's method tells us that it is necessary to choose a short time period wherein we can assume a constant pressure gradient during the production of the well. Since production data usually are intermittent in nature and often have periodic fluctuations, we had to find data sets that had significant stable periods. Of the 128 wells documented in the database that belong to the Salton Sea field operated by CalEnergy, we use six wells for our liquid-dominated case.

Figure 3.1 and 3.2 are examples of steam and water productions histories from Coleman 4-5, a Geysers well, and IDD – 9, a well from the Salton Sea geothermal field.

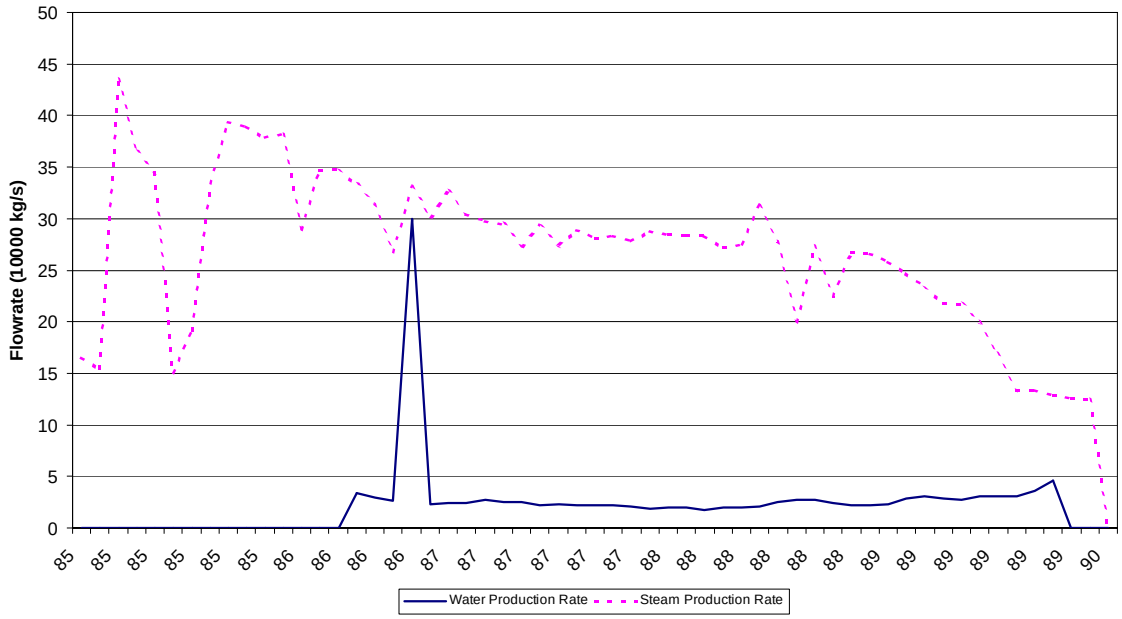

Figure 3.1: Steam and Water Production History of Coleman 4-5, The Geysers Geothermal Field.

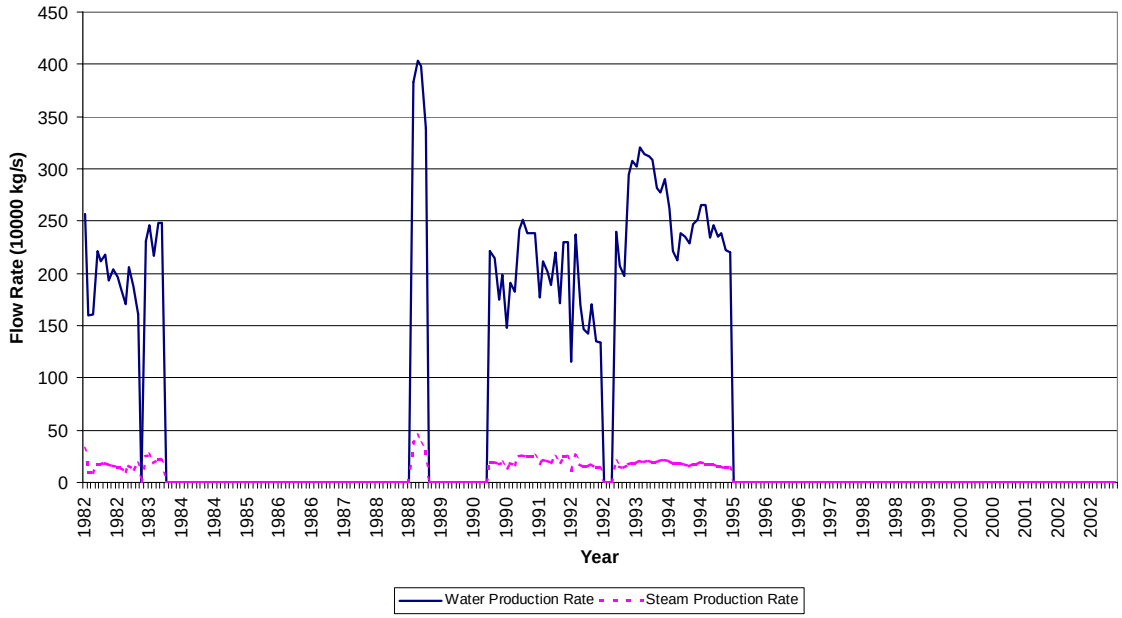

Figure 3.2: Steam and Water Production History of IID - 9, Salton Sea Geothermal Field

Well IDD-9 (Figure 3.2) from Salton Sea had zero production for much of its history. We therefore chose an interval that we can assume to have a constant roughly pressure gradient. For this work we chose a mid-1990 to late-1992 interval.

Choosing the time interval for the vapor-dominated well is much easier. We chose from the mid-1986 to 1989 readings. We try to omit extreme readings from our analysis,

therefore the spike seen in 1986-1987 was not part of the range. For this work, we took a mid-1987 to 1989 interval.

Figures 3.3 and 3.4 show the Q vs Q_w/Q_s graphs for Coleman 5-5 and IDD – 9, respectively. The value of Q^* is inferred from the y-intercept value from the linear fit to the graph. Table 3.1 shows the Q^* inferred from all the wells used in the study.

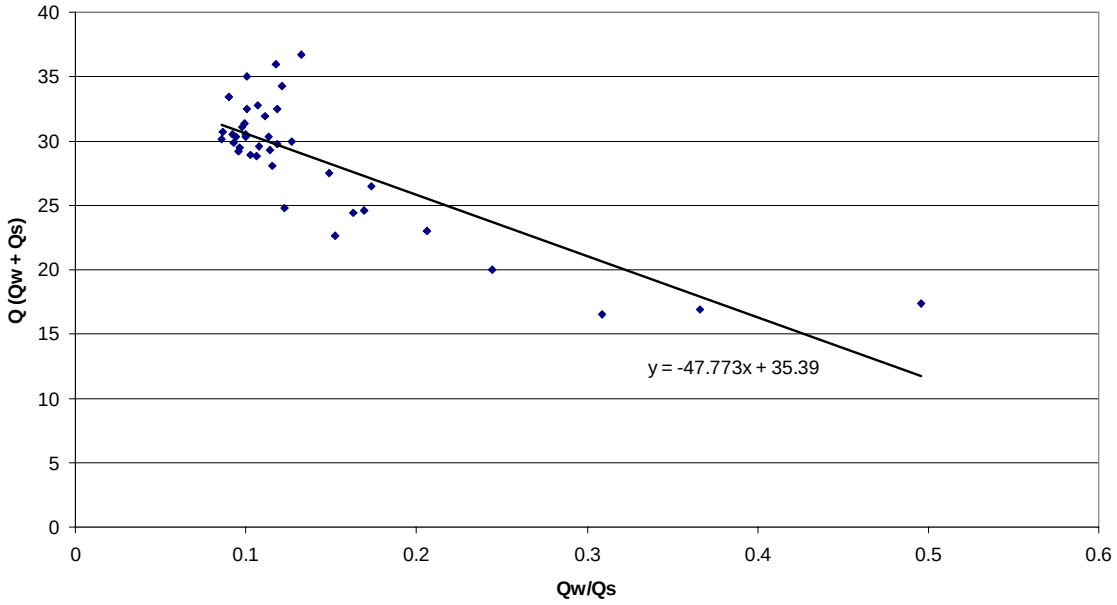

Figure 3.3: Q vs. Q_w/Q_s to infer Q for Coleman 4-5, The Geysers Geothermal Field.*

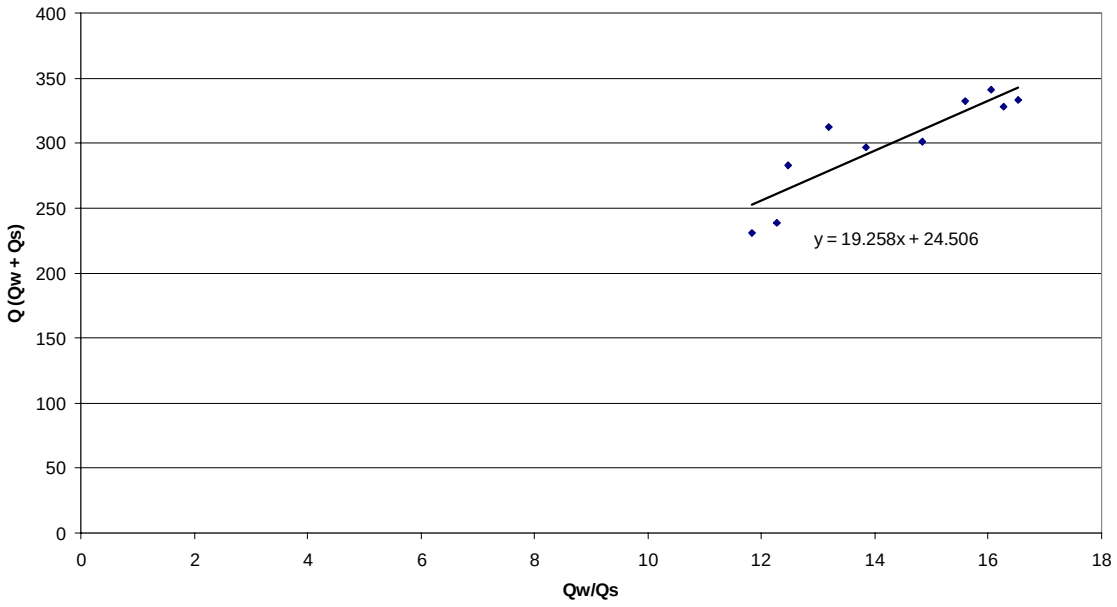

Figure 3.4: Q vs. Q_w/Q_s to infer Q for IID - 9, Salton Sea Geothermal Field.*

Table 3.1: Inferred Q values for the Geysers and Salton Sea Geothermal Field Wells*

Name of Well	Q*
Geysers Wells	
Coleman 4-5	35.39
Coleman 5-5	35.649
Coleman 3-5	24.186
Francisco 2-5	24.182
Coleman 1A-5	24.09
Thorne 6	33.59
Thorne 1	17.384
Francisco 5-5	23.52
CA-5636 6.8E-20	27.868
Salton Sea Wells	
IID – 9	100
Sinclair 20	75
Vonderahe 1	437.56
Sinclair 10	298.62
Elmore 100	200
Sinclair 11	256.5

If we compare the *Q** values between the Geysers wells and the Salton Sea wells, we can see that the Geysers's *Q**values are smaller than the Salton Sea values. Also, the Geysers's *Q** values are near each other. This is an extension of the second assumption made by Shinohara in developing his method. Not only is *kAp'* constant in a well, wells that are near each other or belong to the same geothermal field also have similar *kAp'* values. Since the wells in a certain geothermal field mainly have the same *k* values, and to a certain extent, *A* and *p'*, then our inferred values are consistent with each other. The Salton Sea values have a wider range of values, but are generally in the same larger magnitude compared to the Geysers'.

To correctly evaluate the kinematic viscosities and mass production rates of the steam and water, we must infer the bottomhole conditions of the wells, as this reflects the true flowing conditions of the well. We made temperature corrections based on the documented depths of the wells.

3.4 RESULTS AND DISCUSSION

We can now use Equations 3.6 and 3.7 to calculate the relative permeabilities of steam and water. Figure 3.5 and 3.6 shows us a plot of relative permeability with water saturation for the Geysers and Salton Sea geothermal wells, respectively. Note that these graphs are pltted against the mobile saturation, S*, as defined by Equation 3.5. The mobile saturation excludes the immobile water and steam fractions.

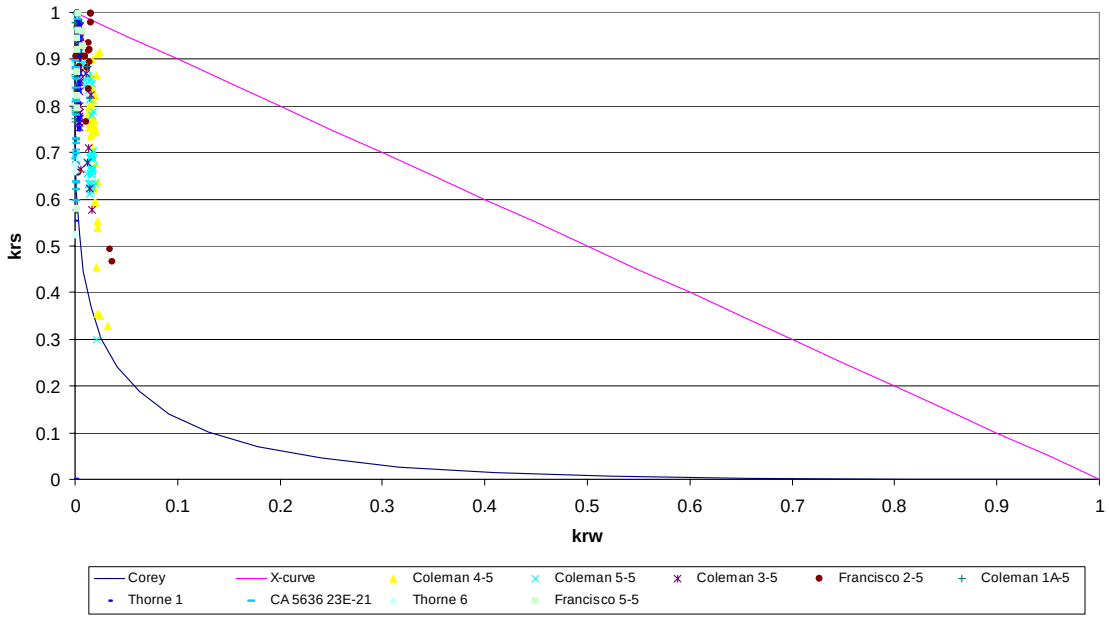

Figure 3.5: Plot of relative permeability curves against water saturation for The Geysers Geothermal Reservoir Field.

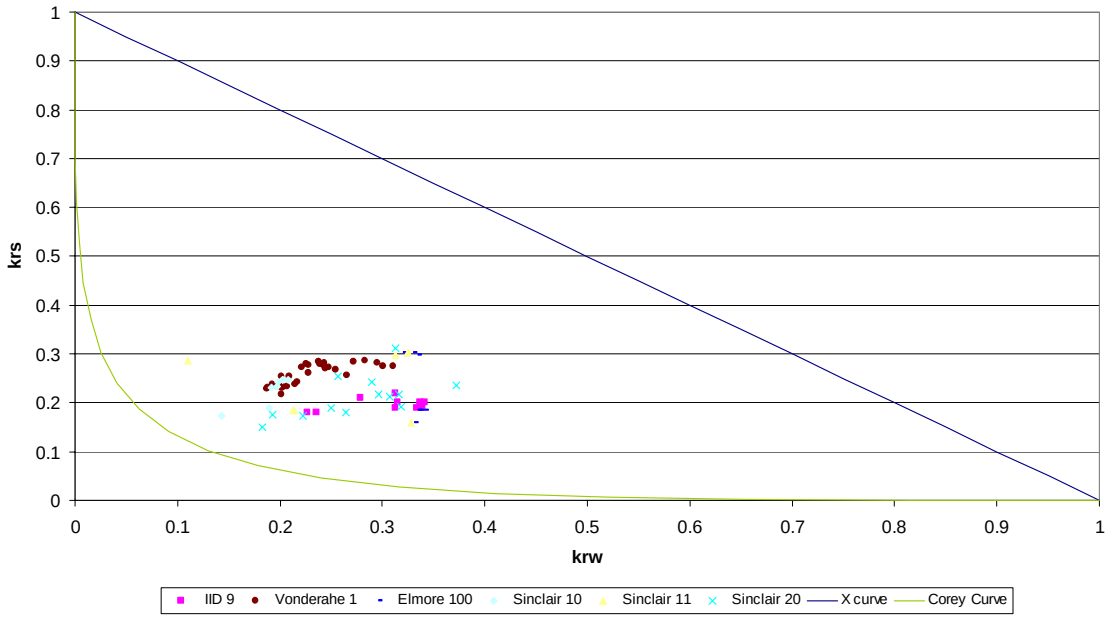

Figure 3.6: Plot of relative permeability curves against water saturation for the Salton Sea Geothermal Reservoir Field.

Figure 3.5 shows us The Geysers relative permeability plot. Because The Geysers is vapor-dominated reservoir, we expected the low water saturation values that are calculated. Figure 3.6, the Salton Sea examples, shows us a larger range for water saturation, with a maximum at around 0.25. Even with a vapor-dominated reservoir, we see that,

volumetrically, the steam saturation values still dominate, even if, by mass, water production has the larger portion.

We try to see the general trend of the relative permeability curves by plotting both well samples into Figure 3.7.

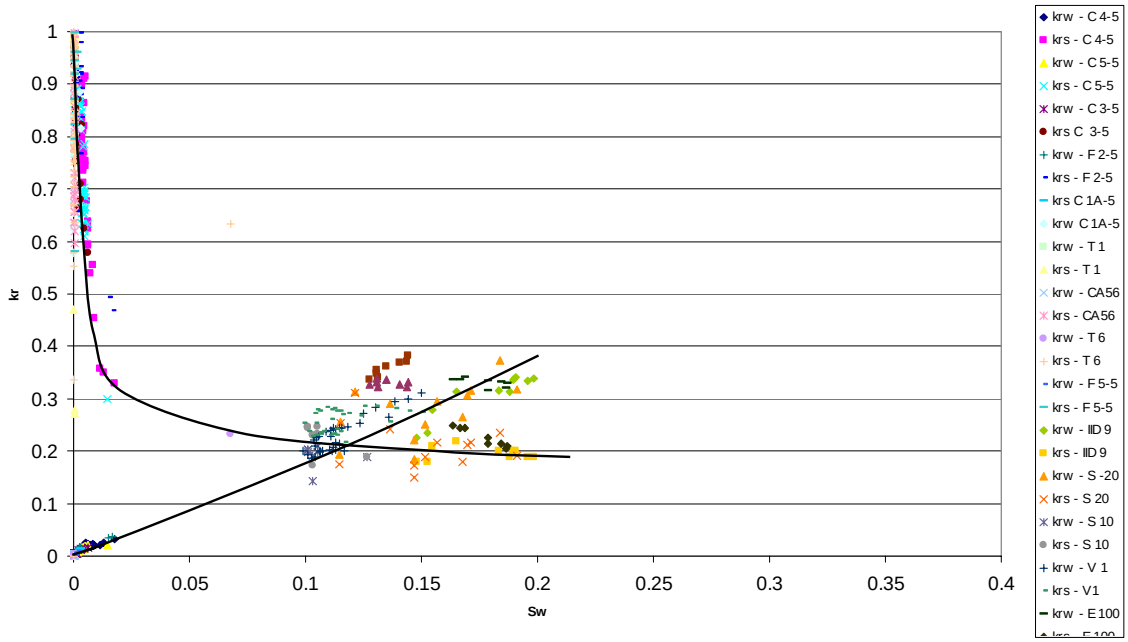

Figure 3.7: Plot of relative permeability curves against water saturation for The Geysers and Salton Sea Geothermal Reservoir Fields.

We see that the relative permeability values for the vapor-dominated and liquid-dominated samples are somewhat consistent with each other. For the relative permeability for steam, the Geysers calculation gives us a sharp drop in k_{rs} at small values of S_w. We then see a plateau of values approaching S_w = 0.1 from the Salton Sea values. For the relative permeability of water, we see a more constant and stable rise as the water saturation also rises. The steepness of the rise for both set of well samples are consistent.

To compare the relative permeability values calculated with the two most commonly assumed models of relative permeabilities, namely Corey and X curves, we plot the computed k_{rw} and k_{rs} values with these model curves. Figure 3.8 and 3.9 show the plots k_{rw} vs. k_{rs} of for the Geysers and Salton Sea well samples, respectively.

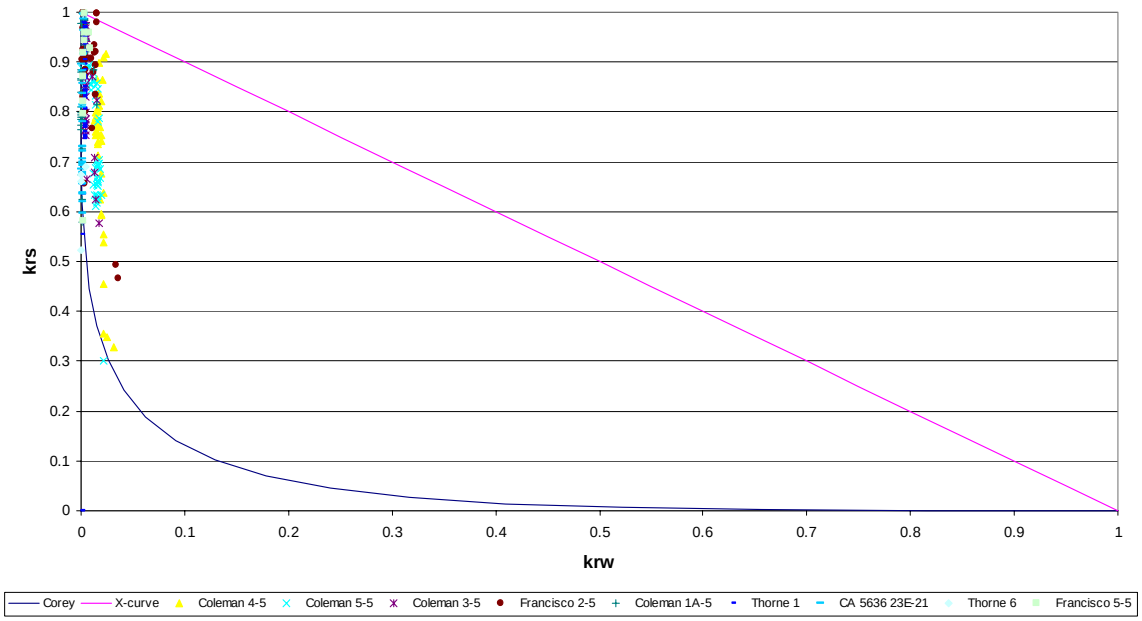

Figure 3.8: Plot of k_{rw} vs k_{rs} for The Geyser's Geothermal Reservoir Field, with the Corey and X-curves.

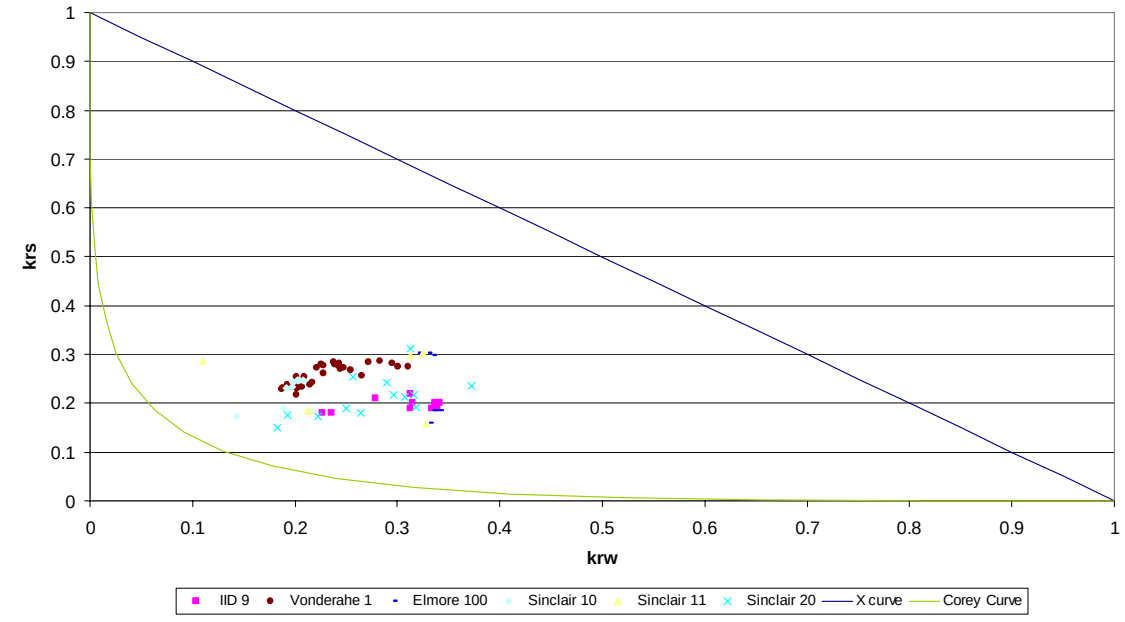

Figure 3.9: Plot of k_{rw} vs k_{rs} for the Salton Sea Geothermal Reservoir Field, with the Corey and X-curves.

For The Geysers samples, we see that the relative permeability follows the Corey-curve relationship. Wee see, as we saw from Figure 3.7, that k_{rs} sharply drops at earlier values, this time for k_{rw}. Figure 3.8 shows the Salton Sea values are more in the middle of the X-curve and Corey-curve. We also see that k_{rs} increases more slowly compared to the rise of k_{rw}. As this happens, the curve goes from the X-curve and approaches the Corey-curve.

In terms of phase interference, we see that at low water saturation, steam relative permeability drops sharply, suggesting that the presence of water greatly interferes with the flow of steam. The water did not seem to be affected by the presence of the steam, at least with $S_w < 0.2$, as the increase in relative permeability of water is stable and almost constant. However, the behavior still exhibits more interference than the X-curve, with an almost 1:2 ratio between k_{rw} and S_w.

We plot Figures 3.8 and 3.9 again, this time with logarithmic axes. Figure 3.10 and 3.11 plots these graphs for the Geysers and Salton Sea well samples, respectively.

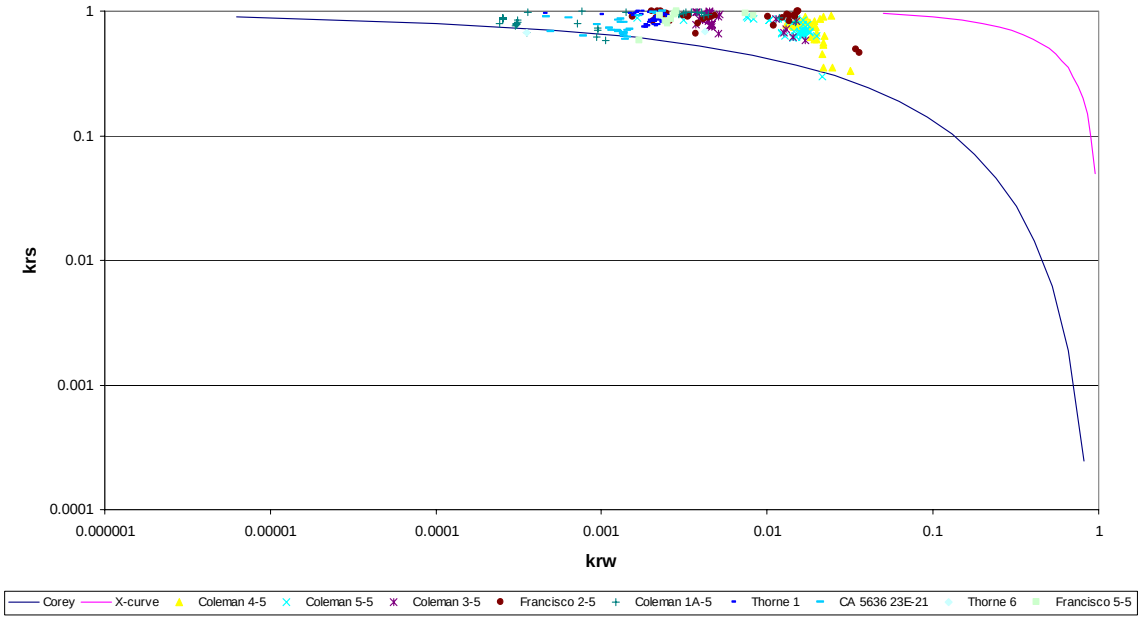

Figure 3.10: Logarithmic plot of k_{rw} vs k_{rs} for the Salton Sea Geothermal Reservoir Field, with the Corey and X-curves.

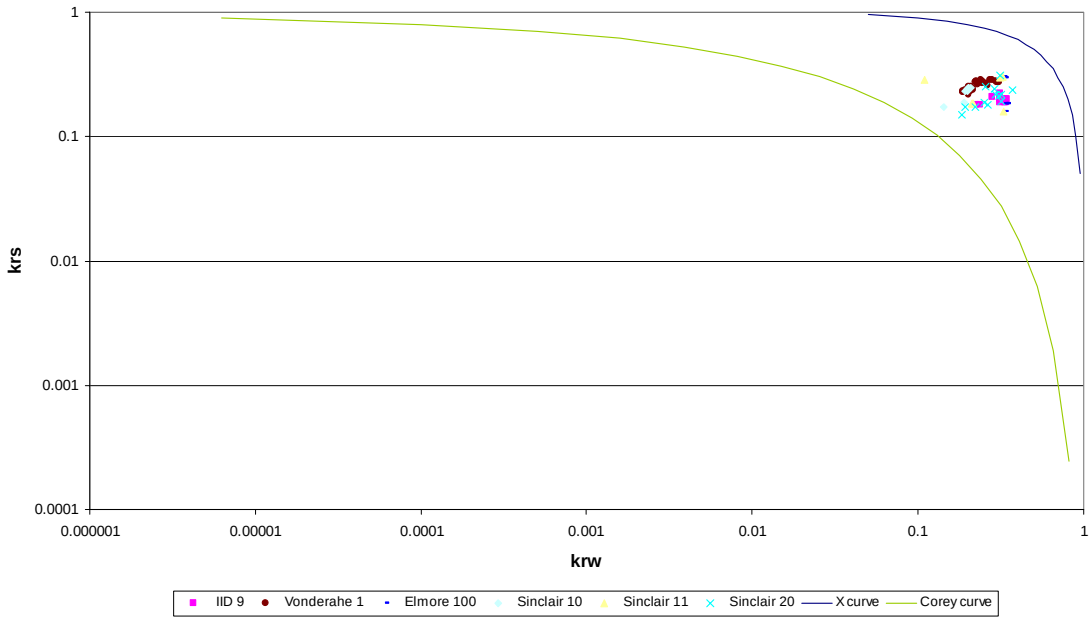

Figure 3.11: Logarithmic plot of k_{rw} vs k_{rs} for the Salton Sea Geothermal Reservoir Field, with the Corey and X-curves.

We see from these two graphs that the calculated values are in the middle of the X- and Corey-curves. Although the relationship we saw in Figure 3.8 cannot be seen in Figure 3.10 because of the difference in scale, we see a somewhat similar relationship between Figures 3.10 and 3.11, wherein the curve approaches the X-curve as S_w increases.

3.5 CONCLUSIONS

1) We can obtain the relative permeabilities from the production flow rate history and bottomhole temperature.
2) There is a sharp decline in the relative permeability of steam at small values of mobile water saturation, and this decline moderates as the saturation increases.
3) The relative permeability of water has a more stable increase compared to the relative permeability of steam.
4) The values of relative permeability follow the Corey-curve at small water saturation values, and then approaches the X-curve as the water saturation increases.

4. REFERENCES

Brooks, R. H. and Corey, A. T.: "Properties of Porous Media Affecting Fluid Flow", *J. Irrig. Drain. Div*., (1966), 6, 61.

Burdine, N. T.: "Relative Permeability Calculations from Pore Size Distribution Data", Trans. *AIME*, (1953), 198, 71.

Chen, C.-Y., Diomampo, G., Li, K. and Horne, R.N.: "Steam-Water Relative Permeability in Fractures," *Geothermal Resources Council Transactions Vol.26*, pp. 87-94, 2002.

Chen, C.-Y., Li, K. and Horne, R.N.: "Difference Between Steam-Water and Air-Water Relative Permeabilities in Fractures," *Geothermal Resources Council Transactions Vol.27*, pp. 793-800, Oct., 2003

Corey, A. T.: "The Interrelation between Gas and Oil Relative Permeabilities", *Prod. Mon*., (1954), **19**, 38.

Diomampo, G., "Relative Permeability through Fractures", MS thesis, Stanford University, Stanford, California (2001).

Fourar, M. and Bories, S.,: "Experimental Study of Air-Water Two-Phase Flow Through A Fracture (Narrow Channel)," *Int. J. Multiphase Flow* Vol. 21, No. 4, (1995) pp. 621-637.

Fourar, M., Bories., Lenormand, R., and Persoff, P.,: "Two-Phase Flow in Smooth and Rough Fractures: Measurement and Correlation by Porous-Medium and Pipe Flow Models," *Water Resources Research* Vol. 29 No. 11. November 1993, pp. 3699-3708.

Fourar, M., and Lenormand, R.,: "A Viscous Coupling Model for Relative Permeabilities in Fractures," Paper SPE 49006, Presented at the SPE Annual Technical Conference and Exhibition, New Orleans, Louisiana, USA, September 27-30, 1998.

Friesen, W.I. and Mikula, R.J.: "Fractal Dimensions of Coal Particles", *J. of Colloid and Interface Science*, V. 120, No.1, November 1987.

Li, K. and Horne, R.N.: "An Experimental and Theoretical Study of Steam-Water Capillary Pressure," *SPEREE* (December 2001), p.477-482.

Li, K. and Horne, R.N.: "Fractal Characterization of The Geysers Rock," Proceedings of the GRC 2003 annual meeting, October 12-15, 2003, Morelia, Mexico; GRC Trans. V. 27 (2003).

Persoff, P. K., Pruess, K., and Myer, L.: "Two-Phase Flow Visualization and Relative Permeability Measurement in Transparent Replicas of Rough-Walled Rock Fractures," *Proc. 16th Workshop on Geothermal Reservoir Engineering*, Stanford University, Stanford, California, January 23-25, 1991.

Persoff, P., and Pruess, K.: "Two-Phase Flow Visualization and Relative Permeability Measurement in Natural Rough-Walled Rock Fractures," *Water Resources Research* Vol. 31, No. 5, May, 1995, pp. 1175-1186.

Purcell, W.R.: "Capillary Pressures-Their Measurement Using Mercury and the Calculation of Permeability", Trans. *AIME*, (1949), 186, 39.

Romm, E.S.: "Fluid Flow in Fractured Rocks", “Nedra” Publishing House, Moscow, 1966 (Translated from the Russian).

Scheidegger, A.E. *The Physics of Flow Through Porous Media*, 3rd ed., University of Toronto, Toronto. 1974.

Shinohara, K., “Calculation and Use of Steam/Water Relative Permeabilities in Geothermal Reservoirs”, MS report, Stanford University, Stanford, California (1978).

Witherspoon, P.A., Wang, J.S.W., Iwai, K. and Gale, J.E.: " Validity of Cubic Law for Fluid Flow in a Deformable Rock Fracture," *Water Resources Research*, Vol. 16, No. 6, 1980, pp 1016-1024.